# *Electronic Supplementary Information*

## Improved performance of the pyrimidine-modified porous In-MOF and an *in situ* prepared composite Ag@In-MOF material

Jing Jin[a], Juanjuan Xue[a], Dan Wu[a], Guoping Yang*[a], and Yaoyu Wang[a]

[a]*Key Laboratory of Synthetic and Natural Functional Molecule of the Ministry of Education, Shaanxi Key Laboratory of Physico-Inorganic Chemistry, College of Chemistry & Materials Science, Northwest University, Xi'an 710127, Shaanxi, P. R. China.*

*E-mail: ygp@nwu.edu.cn.

# Content

## S1. Materials and General Methods

All the chemical reagents used in experiments were purchased commercially that without further purification, and the ligand was bought from Jinan Camolai Trading Company. Elemental analyses of carbon, hydrogen and nitrogen were performed on a PerkinElmer 2400C elemental analyzer. Powder X-ray diffraction (PXRD) data were collected on a Bruker D8 ADVANCE X-ray powder diffractometer (Cu $K\alpha$, $\lambda$ = 1.5418 Å) with $2\theta$ (5−50°). Infrared (IR) spectra were obtained using a BRUKER EQUINOX-55 FT-IR spectrometer KBr pellets in the range of 4000 to 400 $cm^{-1}$. Thermogravimetric analyses (TGA) were measured under a nitrogen stream employing the NETZSCH STA 449C microanalyzer thermal analyzer at a heating rate of 5 ℃ $min^{-1}$. X-ray photoelectron spectroscopy (XPS) measurement was performed on AXIS Ultra spectrometer. The morphology of MOFs was characterized via field emission scanning electron microscope (FESEM S-8010 Hitachi) with an operating voltage of 5 kV. Transmission electron microscopy (TEM) and the corresponding energy-dispersion spectroscopy (EDS) measurements were performed using a microscope (Talos F200X) at 200 kV equipped with an energy dispersive spectrometer. The sorption isotherms were measured by Micrometrics ASAP 2020M. $^{1}$H NMR data were measured on Bruker Ascend 400 spectrometer.

## S2. Experiment Section and Basic Characterization

### S2.1. Crystallographic Data Collection and Refinement

Single-crystal X-ray diffraction data of complexes **1** and **2** were collected on the Bruker SMART APEX II CCD diffractometer equipped with a graphite-monochrome Mo-Kα radiation (λ = 0.71073 Å) at 296 K. Two structures were solved using direct methods and refined by a full-matrix least-squares refinement on $F^2$ with SHELXL-2014 and olex2. The reflection data were corrected by using the SADABS program. Anisotropic thermal parameters were applied to non-hydrogen atoms and all hydrogen atoms from organic ligands were calculated and added at ideal positions. Two structures contained large void, respectively, and the solvent and the positive or negative ions located in the void couldn’t be identified because it was highly disordered had so

small residual peak. Therefore, SQUEEZE in PLATON program was performed to remove the highly disordered solvent and ions. As a result, the hydrogen bond acceptors for the hydroxyls were removed, so the hydrogen bond acceptors for those groups were missing. The final formulas of **1** and **2** were determined by the single-crystal structures, element analysis and TGA. The relevant crystallographic data were depicted in Table S1. Selected bonds lengths and angles were listed in Table S2. The CCDC number is 2079621 for MOF **1** and 2109820 for **2**.

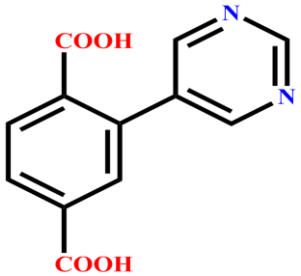


**Scheme S1.** Molecular structure of (2-pyrimidin-5-yl)terephthalic acid ($H_2L$).

**Table S1.** The Crystallographic Data and Structure Refinements for **1** and **2**.

| Complex | 1 | 2 |
|---|---|---|
| Empirical formula | $C_{10}H_6InNO_5$ | $C_8H_5InO_5$ |
| Formula mass | 334.98 | 295.94 |
| Crystal system | Orthorhombic | Orthorhombic |
| Space group | *Cmca* | *Cmca* |
| a [Å] | 21.661(6) | 21.8718(6) |
| b [Å] | 23.081(5) | 23.1289(7) |
| c [Å] | 13.499(3) | 13.5024(3) |
| α [°] | 90 | 90 |
| β [°] | 90 | 90 |
| γ [°] | 90 | 90 |
| V [$Å^3$] | 6749(3) | 6830.5(3) |
| Z | 16 | 16 |
| Dcalcd.[g $cm^{-3}$] | 1.319 | 1.151 |
| μ [$mm^{-1}$] | 1.406 | 1.379 |
| F [000] | 2592 | 2272 |
| θ [°] | 2.579 - 25.587 | 1.979 - 25.410 |
| Reflections collected | 22809 / 3216 | 22232 / 3231 |
| Goodness-of-fit on $F^2$ | 1.114 | 1.073 |
| Final R[a] indices [I>2$\sigma$(I)] | $R_1$ = 0.0502, $wR_2$ = 0.1540 | $R_1$ = 0.0294, $wR_2$ = 0.0777 |
| R indices (all data) | $R_1$ = 0.0667, $wR_2$ = 0.1663 | $R_1$ = 0.0365, $wR_2$ = 0.0822 |

**Table S2.** Selected bond lengths [Å] and angles [ º] for **1-2**.

| **1** | | | |
|---|---|---|---|
| In(1)-O(1)#1 | 2.072(3) | In(2)-O(1)#2 | 2.071(3) |
| In(1)-O(1) | 2.072(3) | In(2)-O(1) | 2.071(3) |
| In(1)-O(3) | 2.162(4) | In(2)-O(2)#2 | 2.143(4) |
| In(1)-O(3)#1 | 2.162(4) | In(2)-O(2) | 2.143(4) |
| In(1)-O(5)#1 | 2.126(4) | In(2)-O(4)#3 | 2.152(4) |
| In(1)-O(5) | 2.126(4) | In(2)-O(4)#1 | 2.152(4) |
| O(1)#1-In(1)-O(1) | 180.0 | O(1)-In(1)-O(5)#1 | 90.35(17) |
| O(1)#1-In(1)-O(3)#1 | 91.85(15) | O(1)#1-In(1)-O(5) | 90.36(17) |
| O(1)-In(1)-O(3)#1 | 88.15(15) | O(1)-In(1)-O(5) | 89.65(17) |
| O(1)-In(1)-O(3) | 91.85(15) | O(3)-In(1)-O(3)#1 | 180.0 |
| O(1)#1-In(1)-O(3) | 88.15(15) | O(5)-In(1)-O(3) | 90.19(17) |
| O(1)#1-In(1)-O(5)#1 | 89.64(17) | O(5)-In(1)-O(3)#1 | 89.81(17) |
| O(5)#1-In(1)-O(3)#1 | 90.19(17) | O(1)#2-In(2)-O(2)#2 | 91.31(15) |
| O(5)#1-In(1)-O(3) | 89.81(17) | O(1)-In(2)-O(2) | 91.31(15) |
| O(5)#1-In(1)-O(5) | 180.0 | O(1)#2-In(2)-O(4)#3 | 93.07(16) |
| O(1)-In(2)-O(1)#2 | 95.9(2) | O(1)-In(2)-O(4)#1 | 93.07(16) |
| O(1)-In(2)-O(2)#2 | 172.72(14) | O(1)-In(2)-O(4)#3 | 91.93(17) |
| O(1)#2-In(2)-O(2) | 172.71(14) | O(1)#2-In(2)-O(4)#1 | 91.93(17) |
| O(2)-In(2)-O(2)#2 | 81.5(2) | O(2)-In(2)-O(4)#1 | 88.60(17) |
| O(2)#2-In(2)-O(4)#1 | 85.74(16) | O(4)#1-In(2)-O(4)#3 | 172.5(2) |
| O(2)-In(2)-O(4)#3 | 85.74(16) | In(2)-O(1)-In(1) | 120.33(18) |
| O(2)#2-In(2)-O(4)#3 | 88.60(17) | | |
| **2** | | | |
| In(1)-O(5) | 2.083(2) | In(2)-O(1)#3 | 2.168(3) |
| In(1)-O(4) | 2.172(3) | In(2)-O(1)#1 | 2.168(3) |
| In(1)-O(2) | 2.152(3) | In(2)-O(3)#1 | 2.150(3) |
| In(2)-O(5) | 2.082(2) | In(2)-O(3)#3 | 2.150(3) |
| O(5)#1-In(1)-O(5) | 95.99(14) | O(5)#1-In(1)-O(2)#1 | 172.57(10) |
| O(5)-In(1)-O(4) | 92.02(11) | O(5)-In(1)-O(2)#1 | 91.36(10) |
| O(5)#1-In(1)-O(4)#1 | 92.02(11) | O(5)-In(1)-O(2) | 172.57(10) |
| O(5)#1-In(1)-O(4) | 93.80(10) | O(4)-In(1)-O(4)#1 | 171.30(15) |
| O(5)-In(1)-O(4)#1 | 93.80(10) | O(2)-In(1)-O(4)#1 | 84.88(10) |
| O(5)#1-In(1)-O(2) | 91.36(10) | O(2)-In(1)-O(4) | 88.52(11) |
| O(2)#1-In(1)-O(4)#1 | 88.53(11) | O(5)-In(2)-O(1)#3 | 87.72(10) |
| O(2)#1-In(1)-O(4) | 84.87(10) | O(5)-In(2)-O(3)#3 | 89.60(11) |
| O(2)-In(1)-O(2)#1 | 81.31(15) | O(5)-In(2)-O(3)#1 | 90.40(11) |
| O(5)#2-In(2)-O(5) | 180.0 | O(5)#2-In(2)-O(3)#1 | 89.61(11) |
| O(5)#2-In(2)-O(1)#1 | 87.72(10) | O(5)#2-In(2)-O(3)#3 | 90.39(11) |
| O(5)-In(2)-O(1)#1 | 92.28(10) | O(1)#1-In(2)-O(1)#3 | 180.0 |

| | | | |
|---|---|---|---|
| O(3)#3-In(2)-O(1)#1 | 89.44(12) | O(3)#3-In(2)-O(3)#1 | 180.00(4) |
| O(3)#1-In(2)-O(1)#1 | 90.56(12) | In(2)-O(5)-In(1) | 118.99(12) |

Symmetry transformations used to generate equivalent atoms: **1**, #1 -x+3/2, -y+1/2, -z+1; #2 -x+3/2, y, -z+1; #3 x, -y+1/2, z-1/2; #4 x, -y+1, -z+1; #5 x+1/2, -y+1/2, -z+1; #6 -x+1, y, z. **2**, #1 -x+1/2, y, -z+1/2; #2 -x+1/2, -y+1/2, -z; #3 x, -y+1/2, z-1/2; #4 -x+1, y, z; #5 x, -y+1, -z+1.

**Table S3.** Comparison of the crystal data for **2** and **MIL-68 (In)**.

| **Compounds** | **2** | **MIL-68 (In)** |
|---|---|---|
| Empirical formula | $C_8H_4InO_5$ | $C_{25}H_{12}In_3O_{15}$ |
| Crystal system | Orthorhombic | Orthorhombic |
| Space group | Cmca | Cmcm |
| *a* [Å] | 21.8718(6) | 21.7739(6) |
| *b* [Å] | 23.1289(7) | 37.677(1) |
| *c* [Å] | 13.5024(3) | 7.2330(1) |
| *α* [°] | 90 | 90 |
| *β* [°] | 90 | 90 |
| *γ* [°] | 90 | 90 |
| *V* [Å$^3$] | 6830.5(3) | 5933.8(2) |

## S2.2. Experiment Section

**Synthesis of {[In(L)$_{0.5}$(bdc)$_{0.5}$(μ$_2$-OH)] ·2H$_2$O}$_n$ (1).** A mixture of $In(NO_3)_3 \cdot 5H_2O$ (0.05 mmol), $H_2L$ (0.05 mmol), $CH_3CN$ (6 mL), $H_2O$ (3 mL) and five drops of $HNO_3$ (1:3) were placed in a 15 mL Teflon-lined stainless steel vessel and then heated at 105 ℃ for three days. After that, the reactor was slowly cool to room temperature, and the transparent flake crystals were obtained. Yield 62% (based on $H_2L$ ligand). IR (KBr, cm$^{-1}$; Fig. S10a†): 3427(m), 2975(w), 1566(s), 1504(m), 1408(s), 1042(w), 908(w), 836(w), 768(m), 719(m), 634(w), 557(m).

**Synthesis of** Ag@**1.** The composite Ag@**1** was obtained by mixing the metal precursor $AgNO_3$ and the raw materials of **1** at 105 ℃ without adding any additional reductant. Different amounts of silver salt from 0.01 - 0.10 mmol were attempted to add into the preparation process of **1**, the results showed that the high-purity composite Ag@**1** was formed successfully when adding 0.05 mmol $AgNO_3$ into the reaction system. Nevertheless, when $AgNO_3$ up to 0.075 mmol, the load of

Ag NPs began to decrease with the appearance of impurities. And the transparent to turbid mother liquor also reflected this difference. Photographs of **1** and Ag@**1** were recorded under the microscope, respectively (Fig. S1†).

**Synthesis of {[In(bdc)($\mu_2$-OH)] 4$H_2O$}$_n$ (2).** The synthesis method of **2** was essentially identical to **1** except for adding 0.05 mmol $H_2$bdc in the synthesis process of **1** or directly using $H_2$bdc in the reaction. And the colorless hexagonal flake crystals were obtained (Fig. S2†). Yield 84% (based on $H_2$bdc). IR (KBr, $cm^{-1}$; Fig. S10b†): 3429(m), 3138(s), 1621(m), 1570(m), 1393(s), 1064(w), 819(w), 762(w), 724(w), 545(w).

**Catalytic Cycloaddition of $CO_2$ with Various Epoxides.** Catalytic cycloaddition reactions were performed by adding **1a**/Ag@**1a** (0.2 mmol) and TBAB (2 mmol) in 15 mL reaction flasks. Epoxides (20 mmol) and $CO_2$ balloons were successively added to the reaction flask after vacuuming, and then studied the catalytic properties at different temperatures and 1 atm. The products were characterized by $^1$H NMR. The exploration of optimal reaction conditions was detailed in Table S4†. And the results showed that the best catalytic efficiency was performed at 80 ℃ and 1 atm.

**Table S4.** The temperature gradient experiments of the $CO_2$ cycloaddition catalyzed by **1a**/TBAB and Ag@**1a**/TBAB, respectively.

| Entry | Catalyst | Epoxides | Products | Temperature | Yield |
|---|---|---|---|---|---|
| **1** | **1a**/TBAB | 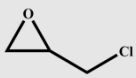 | 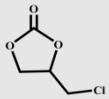 | **25 ℃** | **20.46%** |
| | Ag@**1a**/TBAB | | | | **21.74%** |
| **2** | **1a**/TBAB | 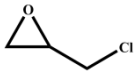 | 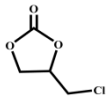 | **40 ℃** | **50.78%** |
| | Ag@**1a**/TBAB | | | | **56.21%** |
| **3** | **1a**/TBAB | 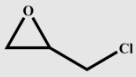 | 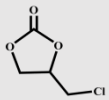 | **60 ℃** | **86.76%** |
| | Ag@**1a**/TBAB | | | | **90.01%** |
| **4** | **1a**/TBAB | 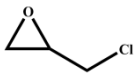 | 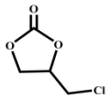 | **80 ℃** | **99.99%** |
| | Ag@**1a**/TBAB | | | | **99.99%** |

## S2.3. Description of the Crystal Structure

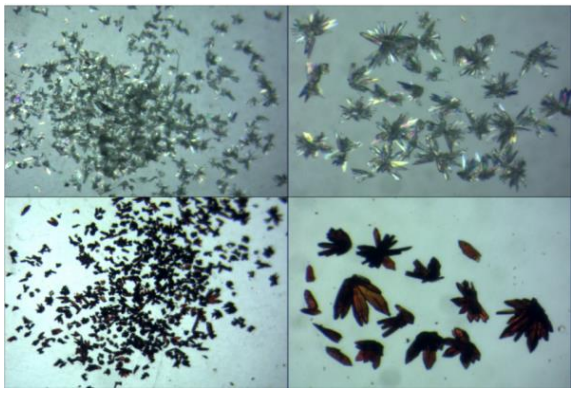

**Fig. S1** The images of **1** and Ag@**1** were recorded under the microscope.

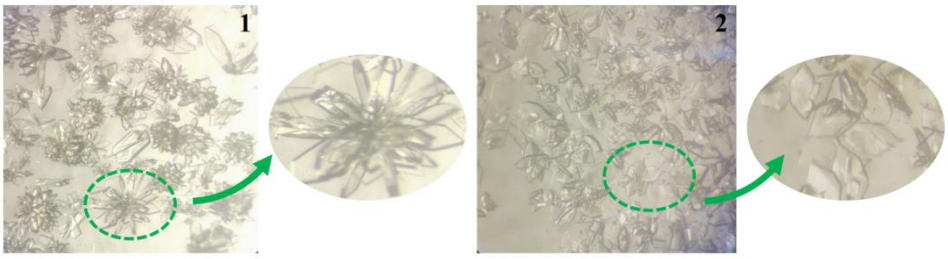


**Fig. S2** The comparison image of crystal morphology for **1** and **2**.

**Structure description of $\{[In(L)_{0.5}(bdc)_{0.5}(\mu_2\text{-}OH)]\cdot 2H_2O\}_n$ (1).** The single-crystal diffraction data shows that **1** exhibits a 3D structure in the orthorhombic system with *Cmca* space group. The asymmetric unit contains one In(III) ion, a half completely deprotonated $L^{2-}$ and $bdc^{2-}$, one bridging $\mu_2$-$OH^-$ anion, and two free water molecules, respectively. As shown in Fig. S3a†, the coordination environment around In1 and In2 is similar, and both are six-coordinate with four O atoms from four $L^{2-}$ ligands and two $\mu_2$-O atoms in an octahedral configuration, respectively. In1 ions are always arranged on the same horizontal line, while In2 ions are distributed among both sides of the In1 axis, and finally In1 and In2 are connected by bridging $\mu_2$-O1 atoms to form an infinite extended zigzag $\{In1\text{-}O1\text{-}In2\}_n$ chain (Fig. S4†). These adjacent 1D chains are connected with $L^{2-}$ to generate a 2D layer (Fig. S3b†), further those layers are joined to other ligands in *c* direction to afford a 3D framework containing 1D open channels decorated by uncoordinated N atoms on the porous surface (Fig. S3c†). Topologically, the framework can be simplified as a 4-connected new net with the point symbol of $(4^2.8^4)$ (Fig. S3d†). Interestingly, the $C(sp^2)$–$C(sp^2)$ $\sigma$ bond between two parts of partial $H_2L$ ligands in the structure of **1** was unexpectedly broken along the horizontal axis on the *c*-section, leading to the formation of 1,4-benzenedicarboxylate

anions ($bdc^{2-}$). It is important that the loss of the pyrimidine ring makes the channels of the framework larger. The effective porosity of **1** is 33.2% regardless of the free solvent molecules.

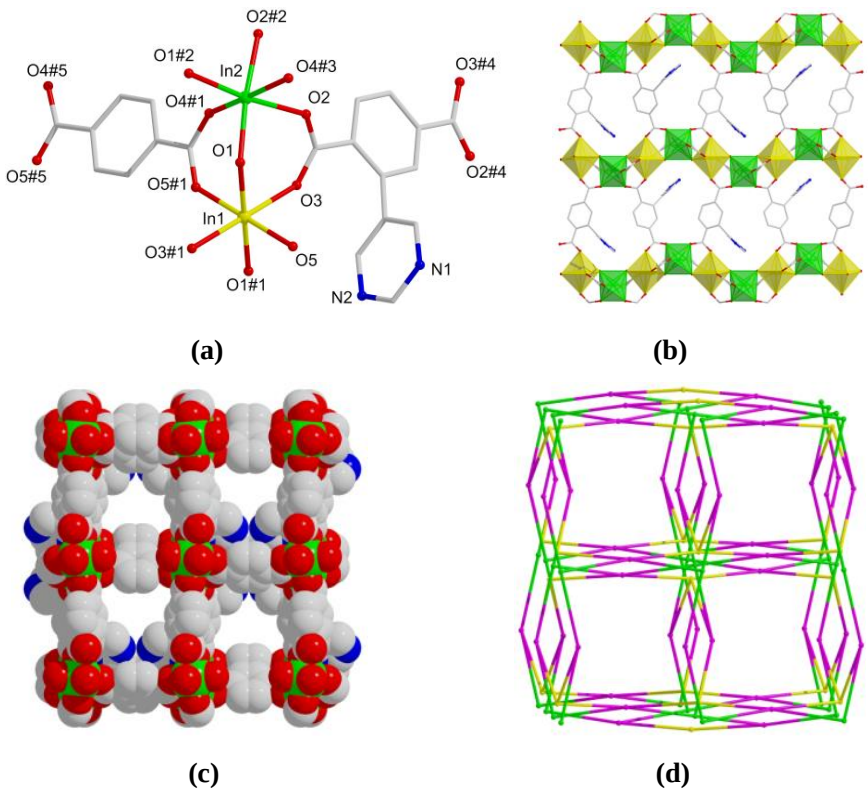


**Fig. S3** (a) Coordination environment of In(III) ions in **1** (In1: yellow, In2: green); (b) 2D layer; (c) The space-filling of 3D framework; (d) The topological net.

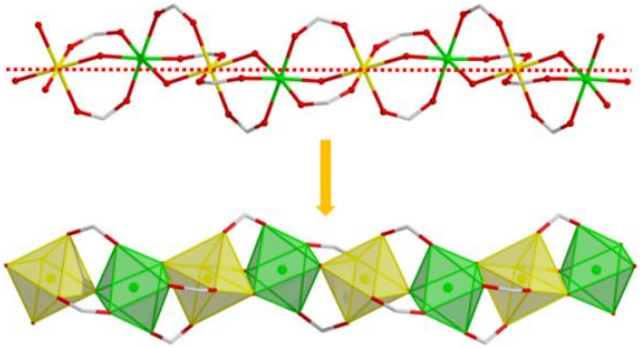

**Fig. S4** The 1D chain of **1** in which In1 and In2 are alternately connected.

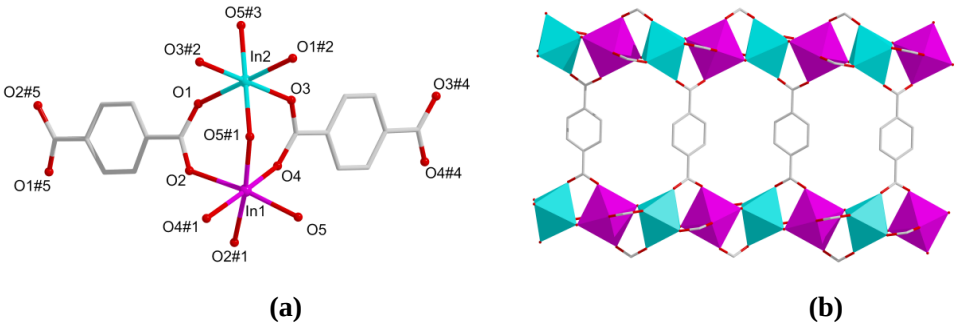

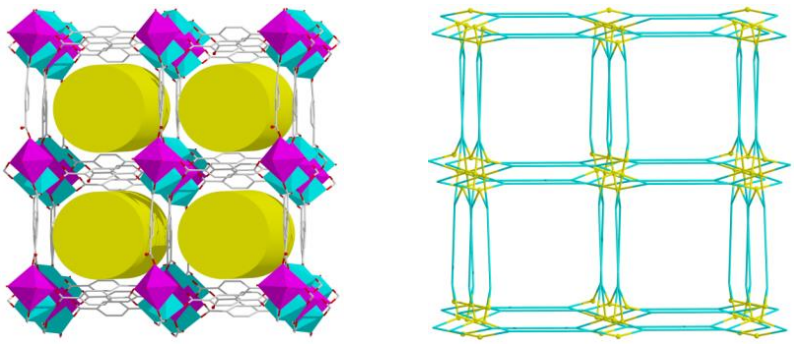

**(c)** **(d)**

**Fig. S5** (a) Coordination environment of In(III) ions in **2** (In1: purple, In2: turquoise); (b) 2D layer; (c) 3D framework; (d) 4-connected topology of **2**.

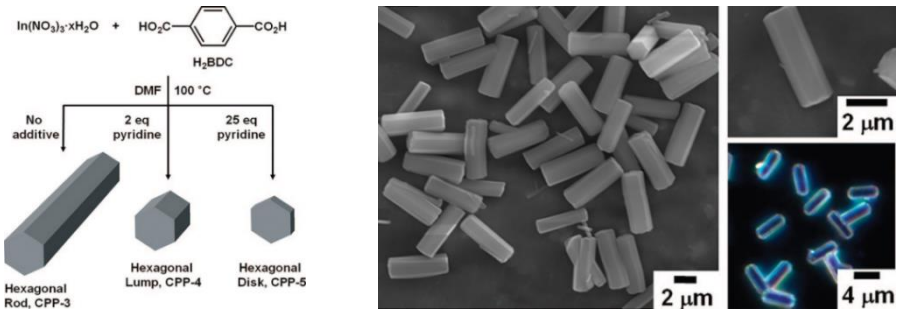


**(a)**

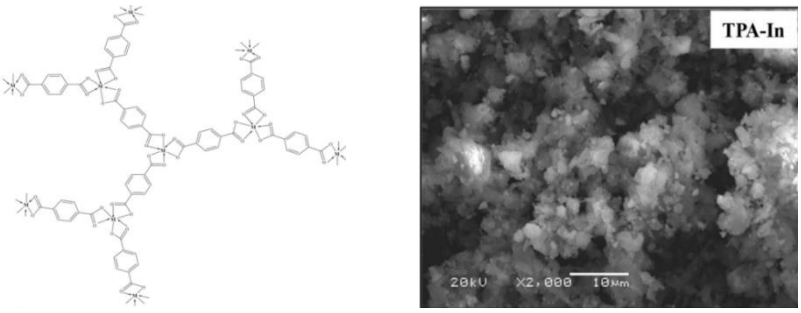


**(b)**

**Fig. S6** (a) Synthetic route and SEM image of hexagonal rods (CPP-3); (b) The schematic representation of TPA-In and SEM image of TPA-In.

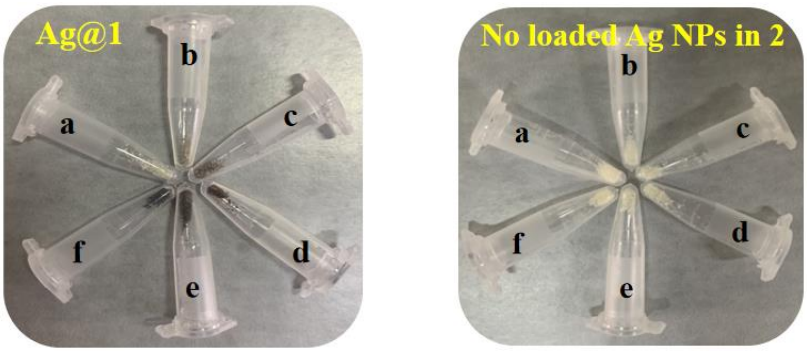


**(a)** **(b)**

**Fig. S7** A comparison photographs of different levels of $AgNO_3$ was introduced into the

complexes **1** and **2**, respectively (a: No added; b: 0.01 mmol; c: 0.025 mmol; d: 0.05 mmol; e: 0.075 mmol; f: 0.10 mmol).

## S2.4. PXRD, TGA and IR

PXRD patterns of **1**, **2** and their processed samples are consistent with their simulated pattern generated from their corresponding single-crystal X-ray diffraction, confirming their high purity and stabilities, respectively (Fig. S8†). Moreover, the TGA curve of **1** reveals that there is a one-step weight loss of 9.93% (calcd 9.73%) below 102 ℃, which corresponds to the release of two free $H_2O$ molecules. After that, the skeleton undergoes a relatively durable stabilization until 428 ℃. In **2**, it displays a weight loss of 20.14% (calcd 19.57%) from 30 - 81 ℃, corresponding to the removal of four lattice $H_2O$ molecules. There existed a plateau in the temperature region of 81 - 420 ℃, while further heating induced an abrupt weight loss due to structural decomposition (Fig. S9†).

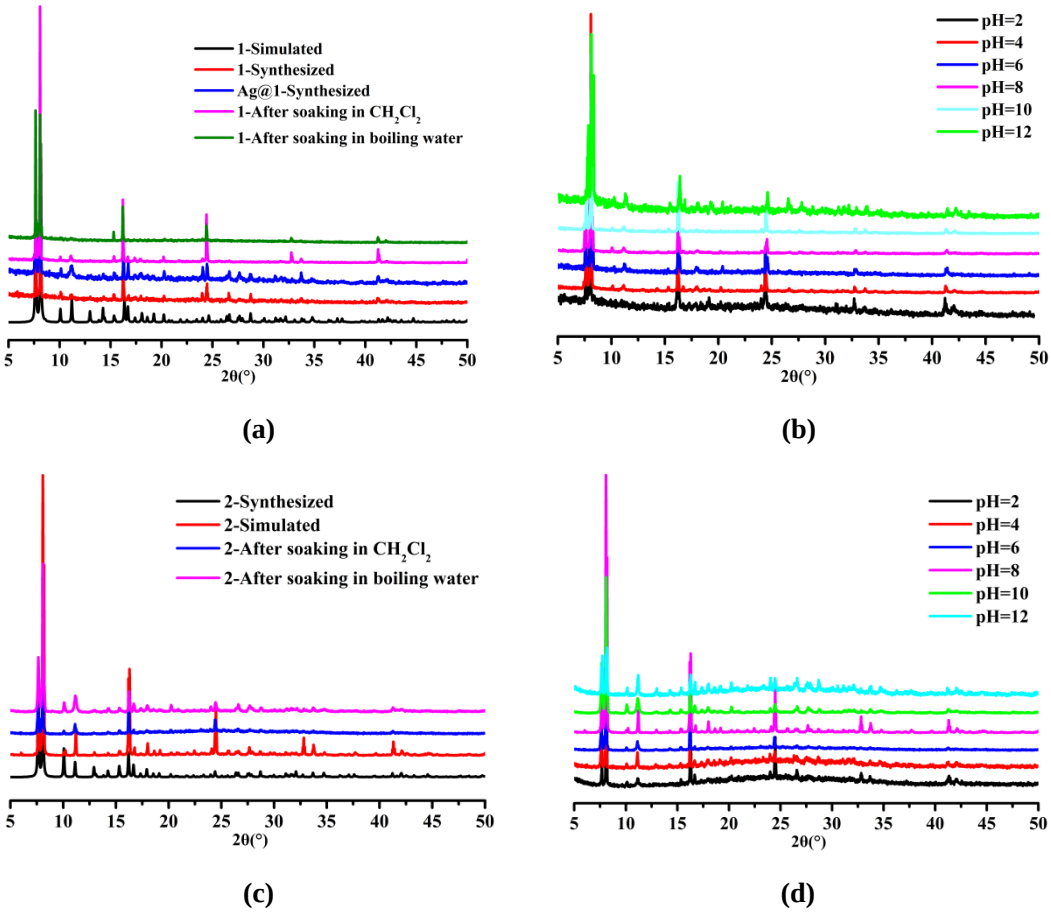


**Fig. S8** (a) PXRD pattern of **1**, Ag@**1**, and **1** after soaking in $CH_2Cl_2$ for three days and boiling water for one day; (b) PXRD pattern of **1** at different pH values; (c) PXRD patterns of **2**, and **2**

after soaking in $CH_2Cl_2$ for three days and boiling water for one day; (d) PXRD pattern of **2** at different pH values.

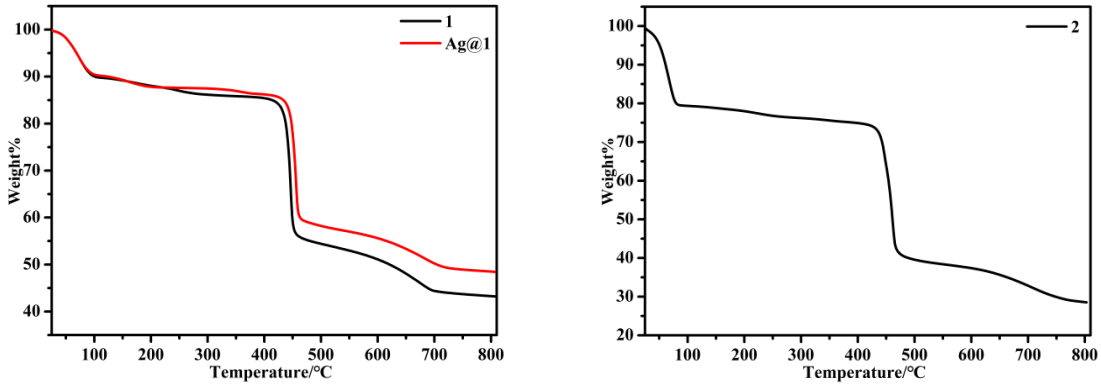


**(a)** **(b)**

**Fig. S9** (a) The TGA curves of **1** and Ag@**1** (a) and **2** (b).

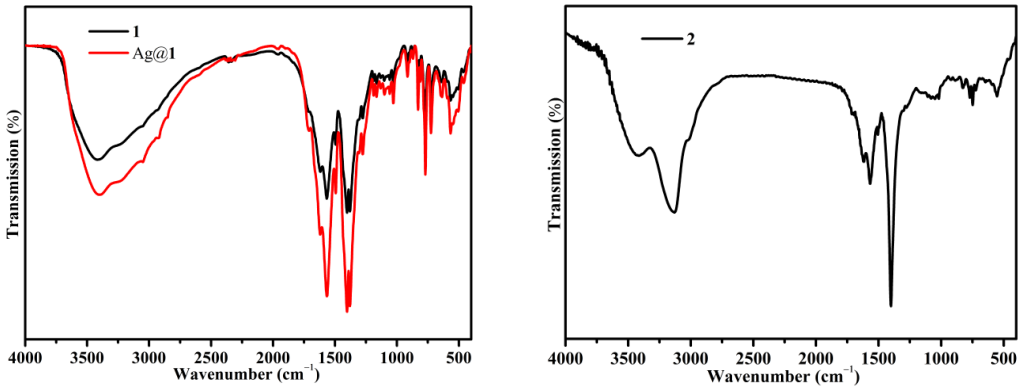


**(a)** **(b)**

**Fig. S10** The FT-IR spectra of **1** and Ag@**1** (a) and **2** (b).

## S3. Characterization of Morphology and Microstructure

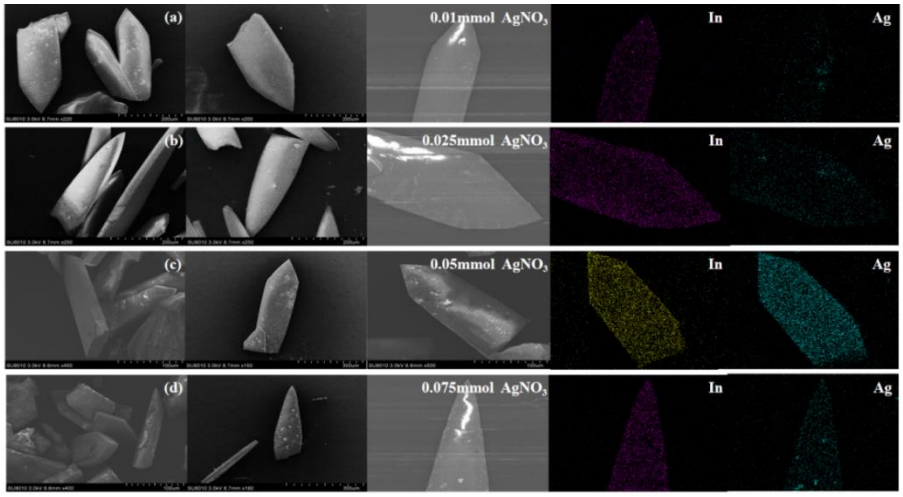


**Fig. S11** The content of Ag element in the composite Ag@**1** synthesized with different content of $AgNO_3$ under SEM.

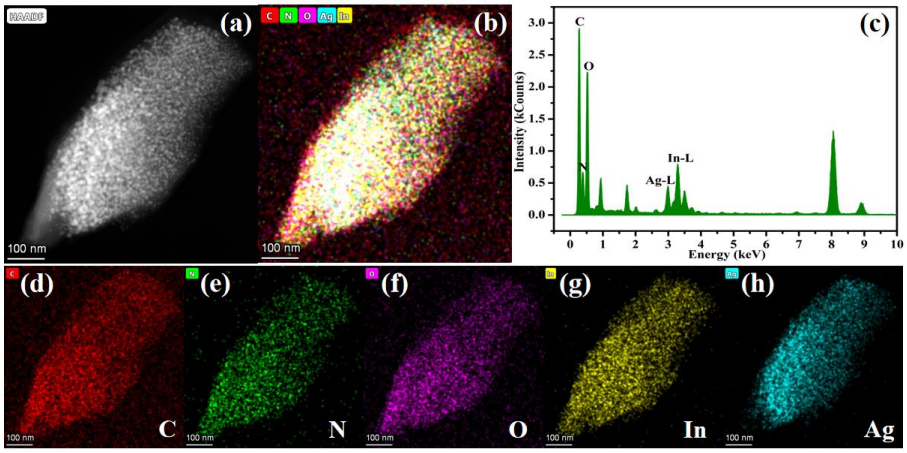


**Fig. S12** (a-b) HAADF-STEM images of Ag@**1**; (c) EDS of Ag@**1**; (d-h) Mapping images of Ag@**1**, and the scale bar is 100 nm. (Element mapping is followed by C, N, O, In, and Ag)

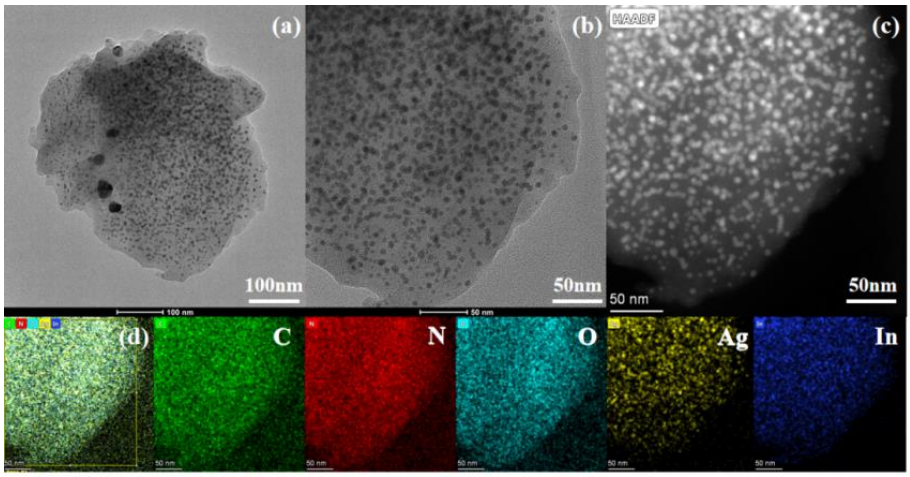


**Fig. S13** TEM images of Ag@**1** after grinding.

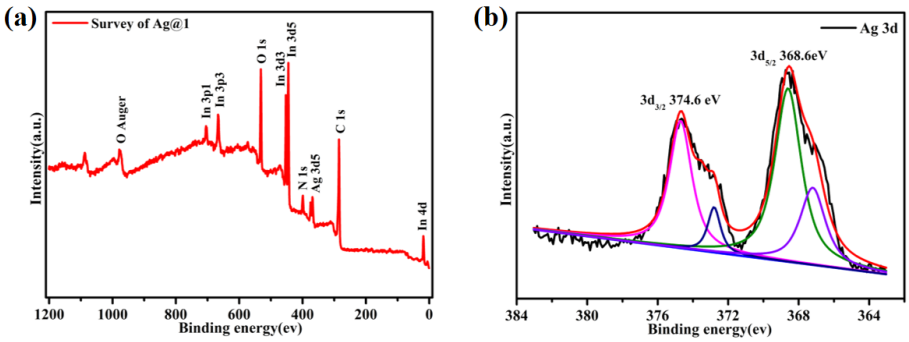


**Fig. S14** (a) Full range XPS spectra of Ag@**1**; (b) XPS spectra of Ag 3d region..

## S4. Gas Adsorption

Since **1** and Ag@**1** have good stability and large 1D channel with uncoordinated sites modification, this encourages us to explore the gas adsorption and separation properties. The

samples were soaked in $CH_2Cl_2$ for three days and then vacuum heat treatment at 200 ℃ to obtain activated samples **1a** and Ag@**1a**. The PXRD patterns determined the stability of those samples (Fig. S15†).

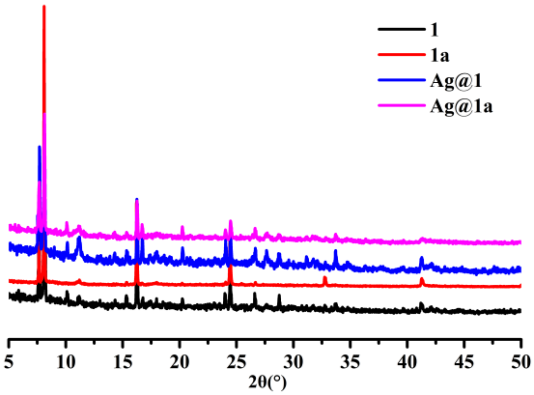


**Fig. S15** PXRD patterns of **1** and Ag@**1** after gas adsorption.

The single-component gases sorption isotherms of $C_2H_2$, $CO_2$, and $CH_4$ are collected at room temperature. Both **1a** and Ag@**1a** display the maximum loading for $C_2H_2$ and the minimum loading for $CH_4$ (Fig. S16a-b†). In detail, the adsorption amounts of **1a** and Ag@**1a** for these gases at 298/273 K are $C_2H_2$ (86.3 and 101.0 $cm^3\ g^{-1}$ for **1a**, 72.6 and 85.9 $cm^3\ g^{-1}$ for Ag@**1a**), $CO_2$ (65.5 and 86.8 $cm^3\ g^{-1}$ for **1a**, 54.5 and 74.2 $cm^3\ g^{-1}$ for Ag@**1a**), and $CH_4$ (20.2 and 30.0 $cm^3\ g^{-1}$ for **1a**, 17.9 and 26.2 $cm^3\ g^{-1}$ for Ag@**1a**), respectively. And the $C_2H_2$ absorption capacity is higher than the most In-MOFs at 298K (Table S5†). The isosteric heat of adsorption ($Q_{st}$) for **1a** and Ag@**1a** are calculated by the virial equation using the adsorption isotherms of 273/298 K (Fig. S21†). The zero-loading adsorption enthalpies of **1a** and Ag@**1a** for $C_2H_2$, $CO_2$, and $CH_4$ are 28.4 and 25.2 kJ $mol^{-1}$, 25.0 and 27.3 kJ $mol^{-1}$, 19.1 and 12.4 kJ $mol^{-1}$, respectively. The $Q_{st}$ value of $C_2H_2$ in **1a** and Ag@**1a** are both higher than many of the reported MOFs, such as BUT-44 (23.1 kJ $mol^{-1}$),[1] ZJU-16a (24.0 kJ $mol^{-1}$),[2] PCM-48 (23.6 kJ $mol^{-1}$),[3] SNNU-63 (21.6 kJ $mol^{-1}$) [4] and Zn-F-DATRZ (20.8 kJ $mol^{-1}$).[5] The high adsorption heat can be attributed to the existence of unsaturated In(III) sites and uncoordinated N atoms in the channels.

**Table S5.** Comparison of $C_2H_2$ adsorption amounts for In-MOFs at 298 K.

| Entry | MOFs | Uptake ($cm^3\ g^{-1}$) | Ref. |
|---|---|---|---|
| 1 | SNNU-150-In | 35.0 | 11 |
| 2 | $[NH_2(CH_3)_2][In(L)_2]$ 2.5DMF 5$H_2O$ | 32.1 | 12 |
| 3 | $(Me_2NH_2)_{1.5}[In_{1.5}(FBDC)(BDC)]$ 2.5NMF $CH_3CN$ | 53.34 | 13 |

| | | | |
|---|---|---|---|
| 4 | $[Me_2NH_2][In(L)]\cdot 2.5NMF\cdot 4H_2O$ | 65.0 | 14 |
| 5 | MROF-12 | 63.25 | 15 |
| 6 | BUT-70A | 65.9 | 16 |
| 7 | $H_3O[In_3(dcpy)_4(OH)_2]\cdot 3DMF\cdot 4H_2O$ | 58.0 | 17 |
| 8 | FJU-6 | 110.0 | 18 |
| 9 | Y-$H_3$TDPAT | 100.0 | 19 |
| **10** | **1a** | **86.3** | **This work** |

Due to the similar trend of adsorption curves between **1a** and Ag@**1a**, and the adsorption capacity of **1a** is higher than that of Ag@**1a**, **1a** is used as a representative to study the selectivity in different molar ratios of $C_2H_2/CH_4$, $CO_2/CH_4$ and $C_2H_2/CO_2$ at 1 atm, which are calculated by the ideal adsorption solution theory (ISAT) at 298 K and are fitted with a theoretical model with the dual-site Langmuir Freundlich (DSLF) equation at 298 K and 1 bar (Fig. S16d-f† and Fig. S18-19†). **1a** shows that the $C_2H_2/CH_4$ selectivity value of the 50/50 mixture is 21.25, which is superior to the reported MOFs in the adsorption selectivity of $C_2H_2/CH_4$.[6-8]

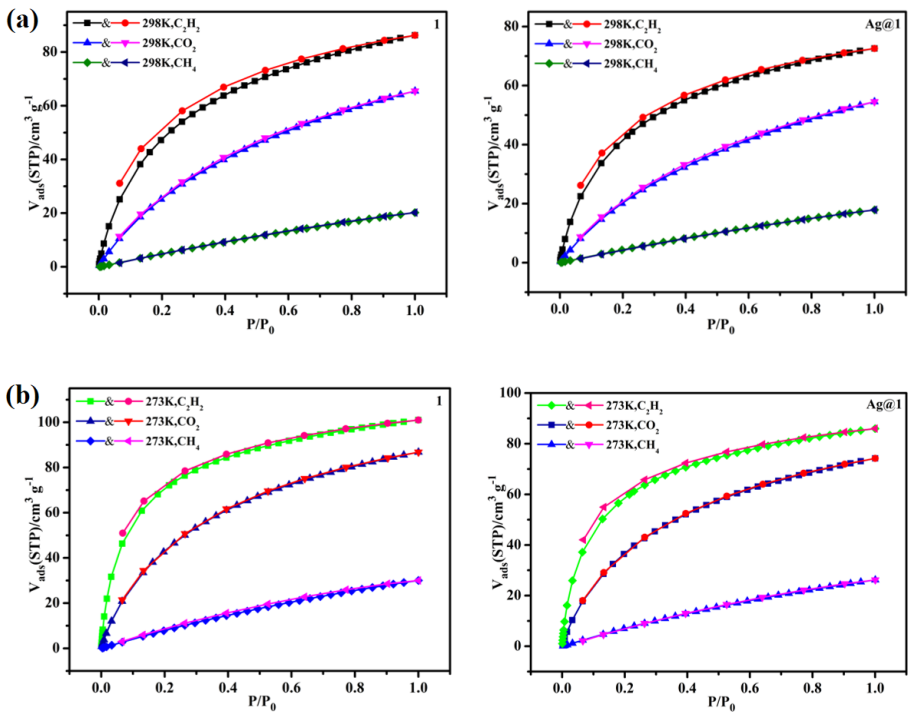

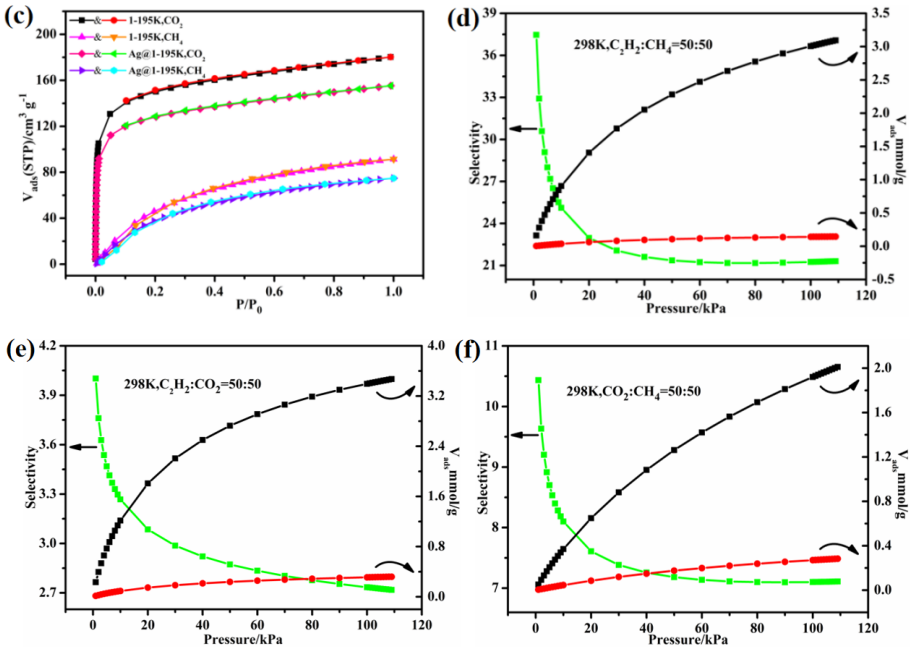


**Fig. S16** $CO_2$, $C_2H_2$ and $CH_4$ sorption and desorption isotherms at 298 K (a) and 273K (b) of **1a** and Ag@**1a**; (c) $CO_2$ and $CH_4$ sorption and desorption isotherms of **1a** and Ag@**1a** at 195 K; (d-f) IAST sorption selectivity of $C_2H_2/CH_4$, $C_2H_2/CO_2$, and $CO_2/CH_4$ for **1a** in equimolar mixtures (50:50) at 298K, respectively.

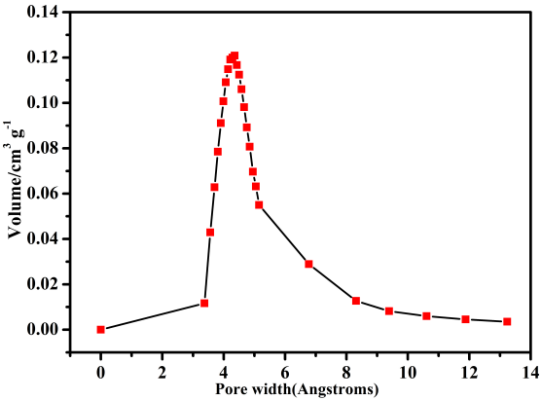


**Fig. S17** Differential pore volume as a function of pore width calculated from the $CO_2$ adsorption isotherm at 195 K of **1a** by using the Horvath-Kawazoe model.

## IAST adsorption selectivity calculation

The experimental isotherm data for pure $C_2H_2$, $CO_2$ and $CH_4$ (measured at 273 and 298 K) were fitted using a Langmuir-Freundlich (L-F) model

$$\mathbf{q} = \frac{\mathbf{a} * \mathbf{b} * \mathbf{p^c}}{\mathbf{1} + \mathbf{b} * \mathbf{p^c}}$$

Where *q* and *p* are adsorbed amounts and pressures of component *i*, respectively. The adsorption selectivities for binary mixtures of $C_2H_2/CH_4$, $CO_2/CH_4$, $C_2H_2/CO_2$ at 273 and 298 K., defined by

$$S_{ads} = (\frac{q1}{q2})/(\frac{p1}{p2})$$

Where *qi* is the amount of *i* adsorbed and *pi* is the partial pressure of *i* in the mixture.

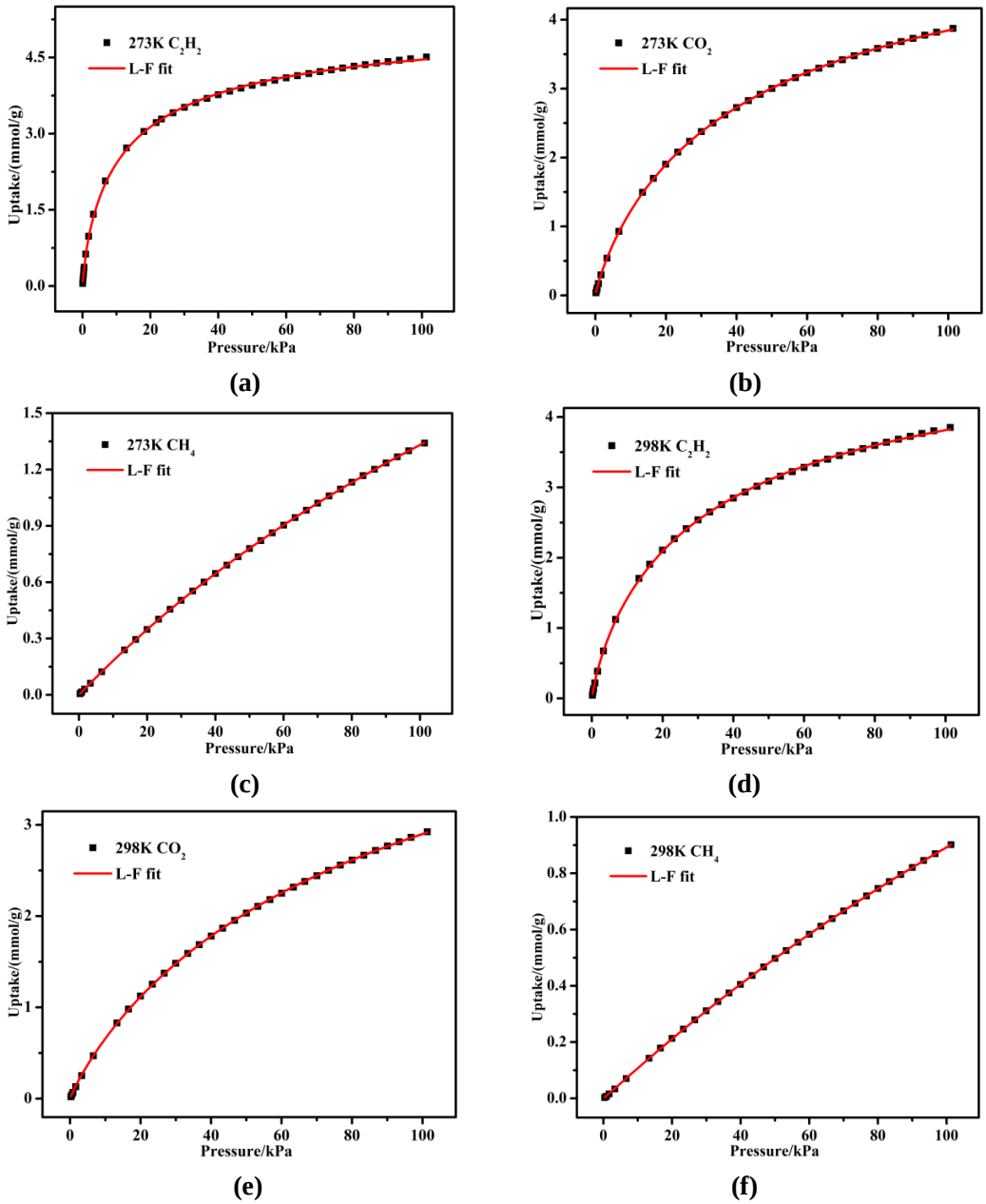


**Fig. S18** (a) $C_2H_2$ adsorption isotherms of **1a** at 273 K with fitting by L-F model: a =5.38353, b =0.13805, c =0.77145, Chi^2 = 8.33363E-4, R^2 = 0.99966. (b) $CO_2$ adsorption isotherms of **1a** at 273 K with fitting by L-F model: a = 5.84385, b =0.03656, c =0.86068, Chi^2 = 5.16033E-5, R^2 = 0.99996. (c) $CH_4$ adsorption isotherms of **1a** at 273 K with fitting by L-F model: a = 4.60954, b = 0.00414, c = 0.99561, Chi^2 = 1.35445E-6, R^2 = 0.99999. (d) $C_2H_2$ adsorption isotherms of **1a** at 298 K with fitting by L-F model: a = 5.45923, b = 0.05372, c = 0.81749, Chi^2 = 2.39951E-4, R^2 = 0.99985. (e) $CO_2$ adsorption isotherms of **1a** at 298 K with fitting by L-F model: a = 0.06947, b = 0.01652, c = 0.89894, Chi^2 = 3.52552E-5, R^2 = 0.99996. (f) $CH_4$ adsorption isotherms of **1a** at 298 K with fitting by L-F model: a = 3.97711, b = 0.00265, c = 1.01874, Chi^2 = 1.15709E-6, R^2 = 0.99999.

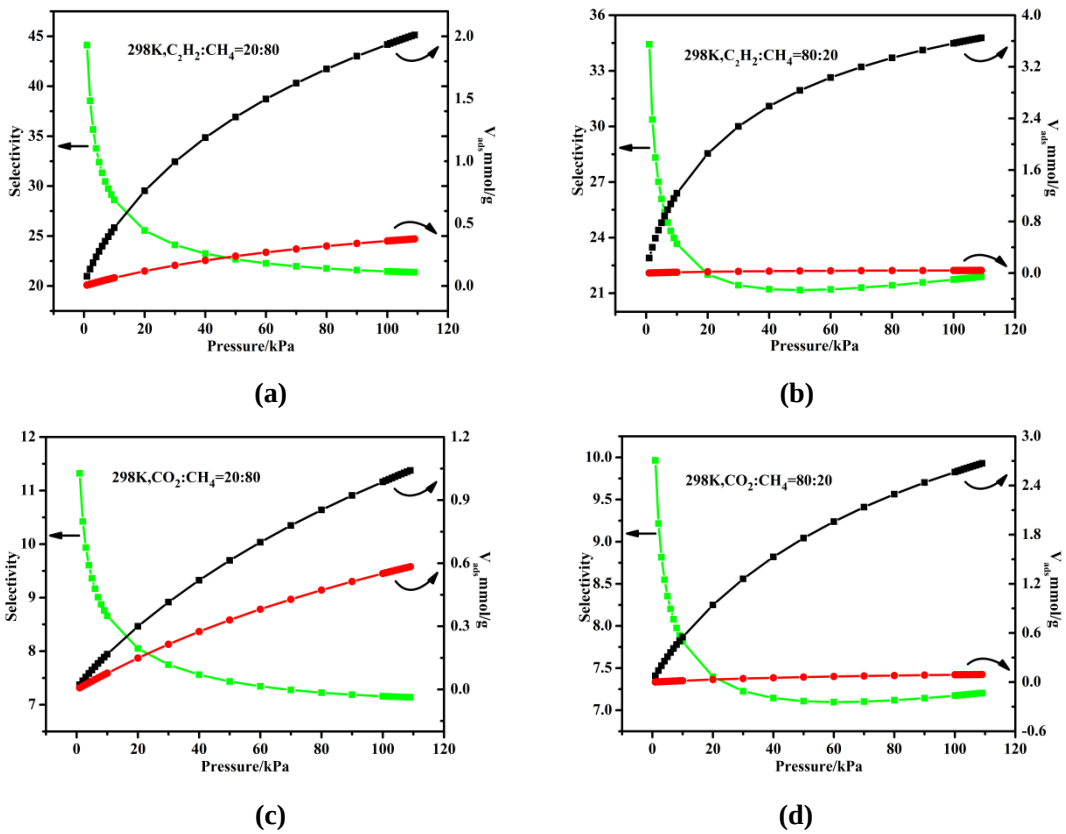


**Fig. S19** IAST adsorption selectivity of **1a** for equimolar mixtures of $C_2H_2$, $CO_2$ and $CH_4$ at 298K, respectively.

### Calculation of sorption heat for $C_2H_2$, $CO_2$ and $CH_4$ uptake using Virial 2 model

The $C_2H_2$, $CO_2$ and $CH_4$ adsorption isotherm data for **1a** at 298 K were fitted using the Virial 2 expression, where $P$ is the pressure, $N$ is the adsorbed amount, $T$ is the temperature, $a_i$ and $b_i$ are virial coefficients, and $m$ and $N$ are the number of coefficients used to describe the isotherms. $Q_{st}$ is the coverage–dependent enthalpy of adsorption and $R$ is the universal gas constant.

$$\ln P = \ln N + 1/T \sum_{i=0}^{m} a_i N^i + \sum_{i=0}^{n} b_i N^i \qquad Q_{st} = R \sum_{i=0}^{m} a_i N^i$$

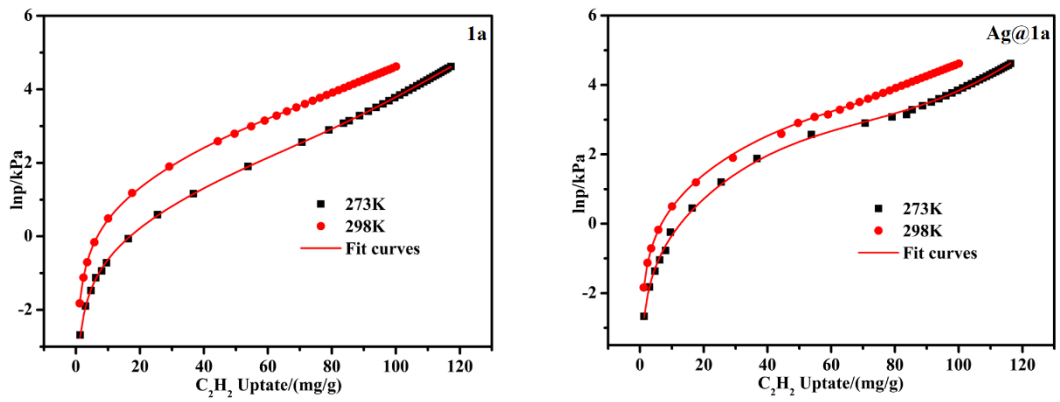

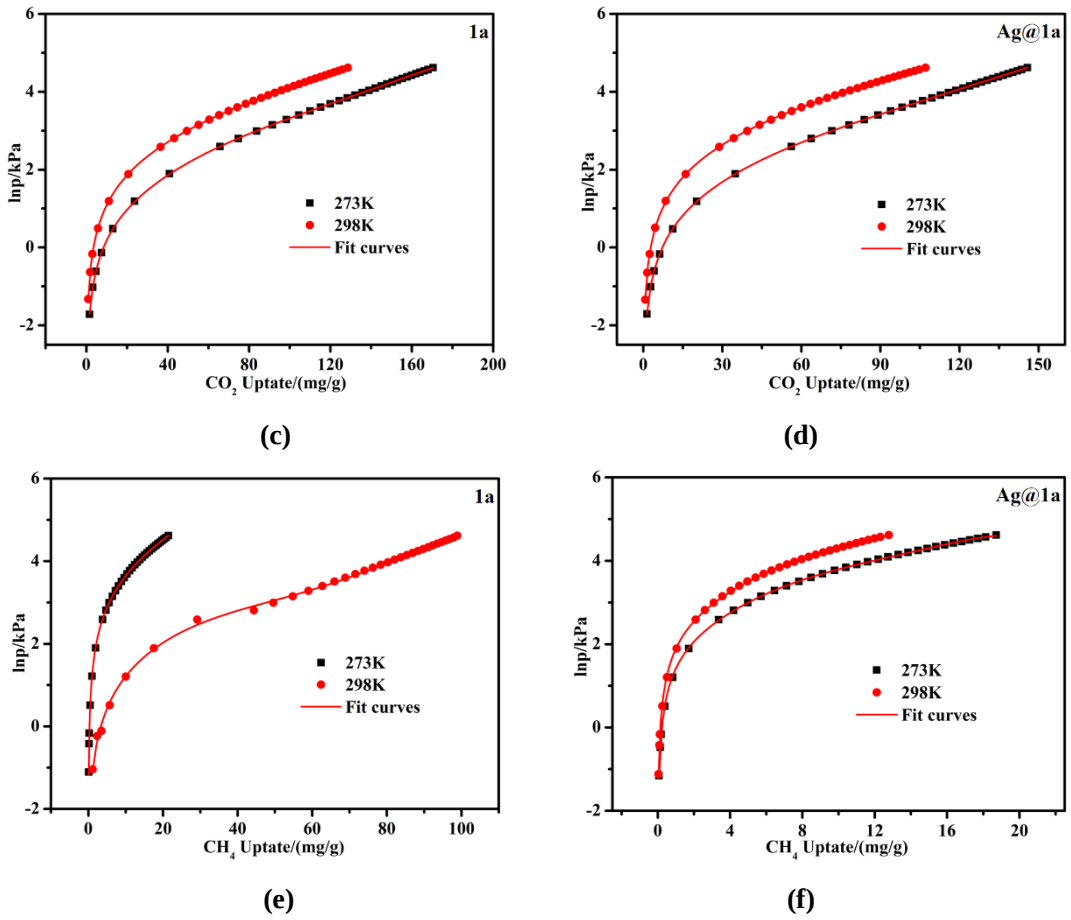


**Fig. S20** (a) $C_2H_2$ adsorption isotherms for **1a** with fitting by Virial 2 model. Fitting results: a0 = -3404.33102, a1 = -14.35413, a2 = 0.34198, a3 = -0.00335, a4 = 2.94704E-5, a5 = -8.91679E-8, b0 = 9.45331, b1 = 0.05542, b2 = -5.85578E-4, Chi^2 = 3.38334E-4, R^2 = 0.99991. (b) $C_2H_2$ adsorption isotherms for Ag@**1a** with fitting by Virial 2 model. Fitting results: a0 = -3088.3626, a1 = 48.48416, a2 = -0.30626, a3 = -0.00491, a4 = 4.77991E-5, a5 = -1.37624E-7, b0 = 8.31337, b1 = -0.14457, b2 = 0.00157, Chi^2 = 0.00306, R^2 = 0.9992. (c) $CO_2$ adsorption isotherms for **1a** with fitting by Virial 2 model. Fitting results: a0 = -3015.78862, a1 = 6.45158, a2 = 0.00245, a3 = -4.4331E-4, a4 = 2.7889E-6, a5 = -5.86924E-9, b0 = 8.84893, b1 = -0.01666, b2 = 9.42737E-5, Chi^2 = 3.78884E-5, R^2 = 0.99999. (d) $CO_2$ adsorption isotherms for Ag@**1a** with fitting by Virial 2 model. Fitting results: a0 = -3283.75263, a1 = 5.96474, a2 = -0.00305, a3 = -8.37658E-5, a4 = 9.84315E-7, a5 = -2.51776E-9, b0 = 9.97037, b1 = -0.01016, b2 = 7.49668E-6, Chi^2 = 4.4435E-5, R^2 = 0.99998. (e) $CH_4$ adsorption isotherms for **1a** with fitting by Virial 2 model. Fitting results: a0 =8150.20691, a1 = -44.23174, a2 = 2.1884, a3 = -0.00349, a4 = 6.98741E-5, a5 = -3.46179E-7, b0 = -28.61711, b1 = 0.16788, b2 =-0.00742, Chi^2 = 0.00174, R^2 = 0.99926. (f) $CH_4$ adsorption isotherms for Ag@**1a** with fitting by Virial 2 model. Fitting results: a0 = -1483.51624, a1 = -68.25241, a2 = 12.40796, a3 = -1.30929, a4 = 0.06756, a5 = -0.00129, b0 = 6.95972, b1 = 0.10283, b2 = -0.00311, Chi^2 = 4.83924E-4, R^2 = 0.9998.

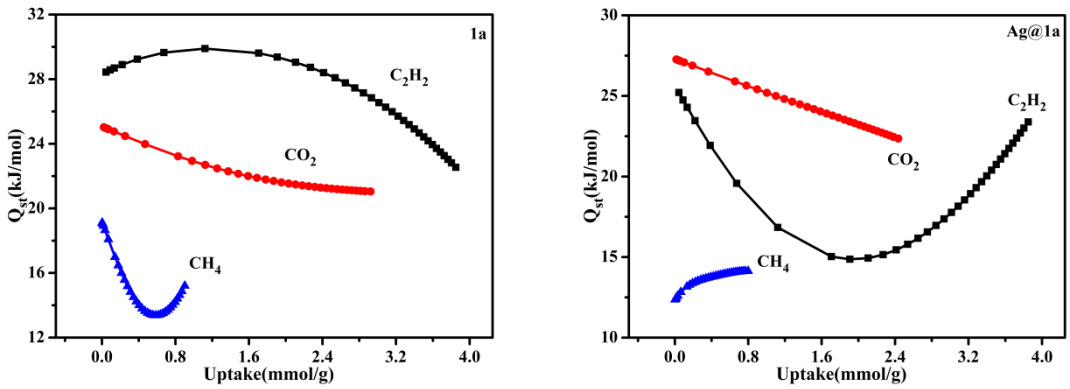


**Fig. S21** Adsorption heat of **1a** and Ag@**1a** for $C_2H_2$, $CH_4$ and $CO_2$, respectively.

## S5. Mechanism of $CO_2$ epoxidation

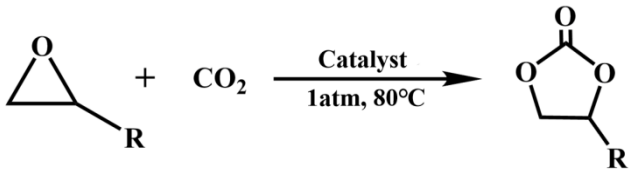


**Scheme S2.** $CO_2$ cycloaddition reaction with different epoxides.

According to the literature, there may be two reaction mechanisms in this study.[9] The first mechanism is that the O atoms of the epoxy substrate interact with unsaturated In(III) centers (Scheme S3a†). At the same time, the $Br^-$ of the co-catalyst TBAB attacks the less sterically hindered carbon atoms in the epoxy substrate, causing the epoxy substrate to open the ring and generate active oxygen anions. Subsequently, the active oxygen anion reacts with $CO_2$ to form an alkyl carbonate anion, and finally a ring-closing reaction produces the corresponding cyclic carbonate and proceeds to the next round of catalysis cyclic. The second catalytic mechanism is considered to be the interaction of the substrate O atom with the Lewis acid sites and the $CO_2$ molecule is simultaneously polarized by the base site (N atoms) (Scheme S3b†). The O atom in the $CO_2$ is converted into an oxygen anion. Then the oxygen anion attacks the less hindered carbon atoms in the epoxide to product an alkyl carbonate anion, and finally, a ring-closing reaction occurs to form the corresponding cyclic carbonate. In addition, compared with 1a, the catalytic performance of Ag@1a was higher than that of 1a because of the synergistic effect between Ag NPs and In(III) centers. According to the similar report in the literature,[10] in the second reaction cycle, Ag NPs can combine with two active oxygen anions produced after ring

opening of the epoxy substrate, and then connect with two $CO_2$ molecules to form alkyl carbonate anions. Then the ring is closed to form two cyclic carbonates coordinated with Ag. Finally, the reaction ends by releasing the cyclic carbonate and the reduction of the catalyst in the medium (Scheme S4†).

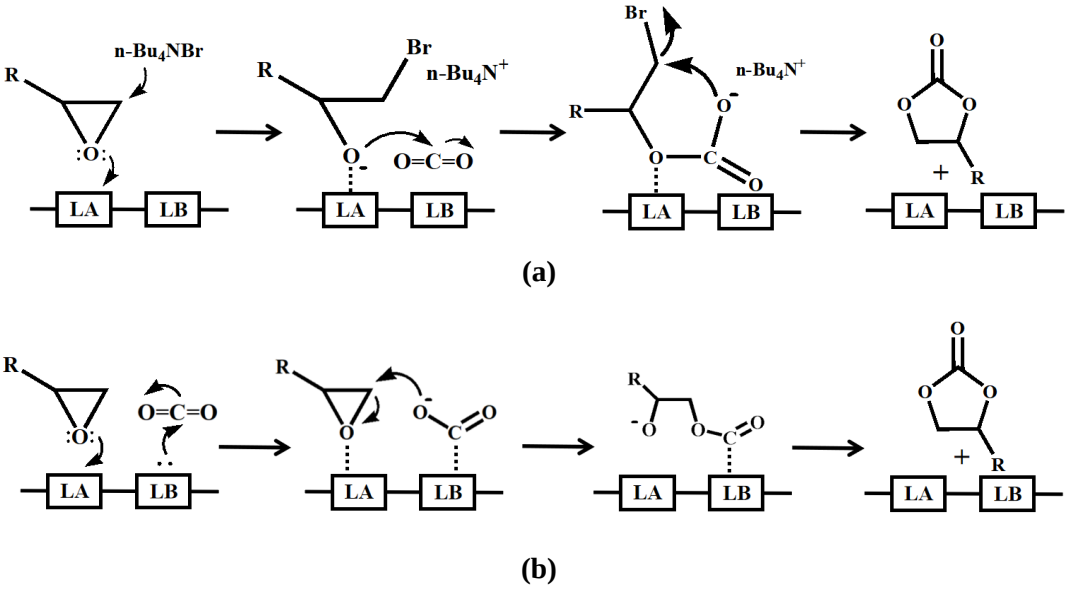


**Scheme S3.** The proposed mechanism of **1a** and Ag@**1a** in catalyzing $CO_2$ cycloaddition reaction.

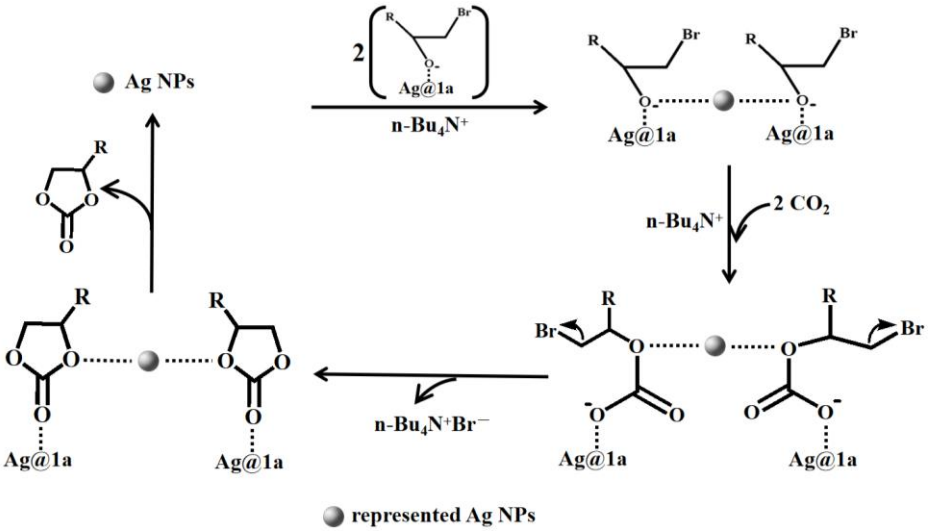


**Scheme S4.** Another proposed mechanism of Ag@**1a** accelerating the catalytic cycloaddition reaction of $CO_2$.

## S6. $^{1}$H NMR Spectrums

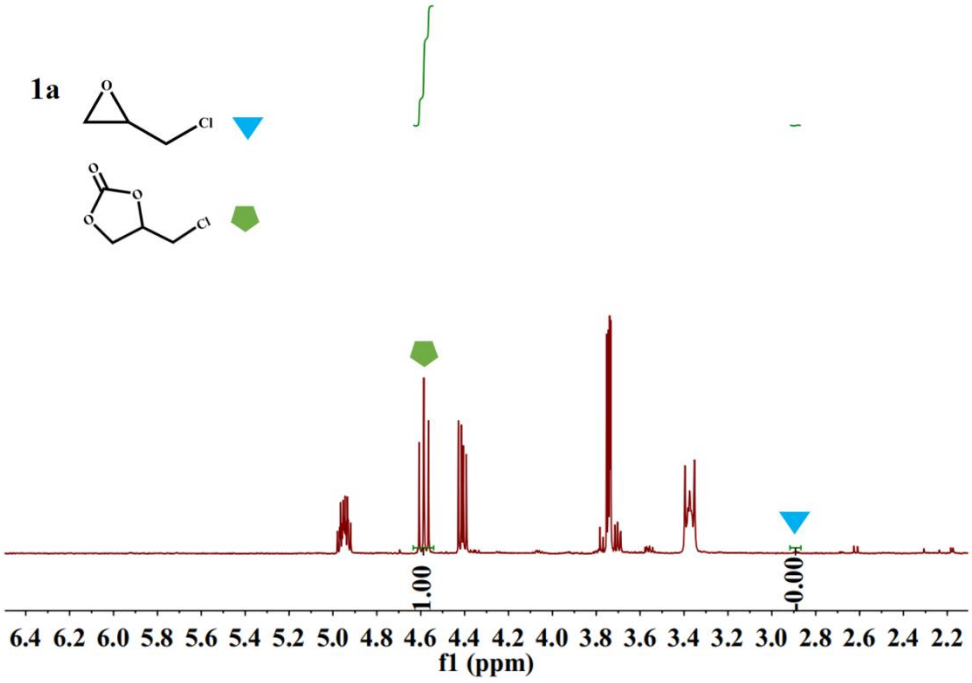


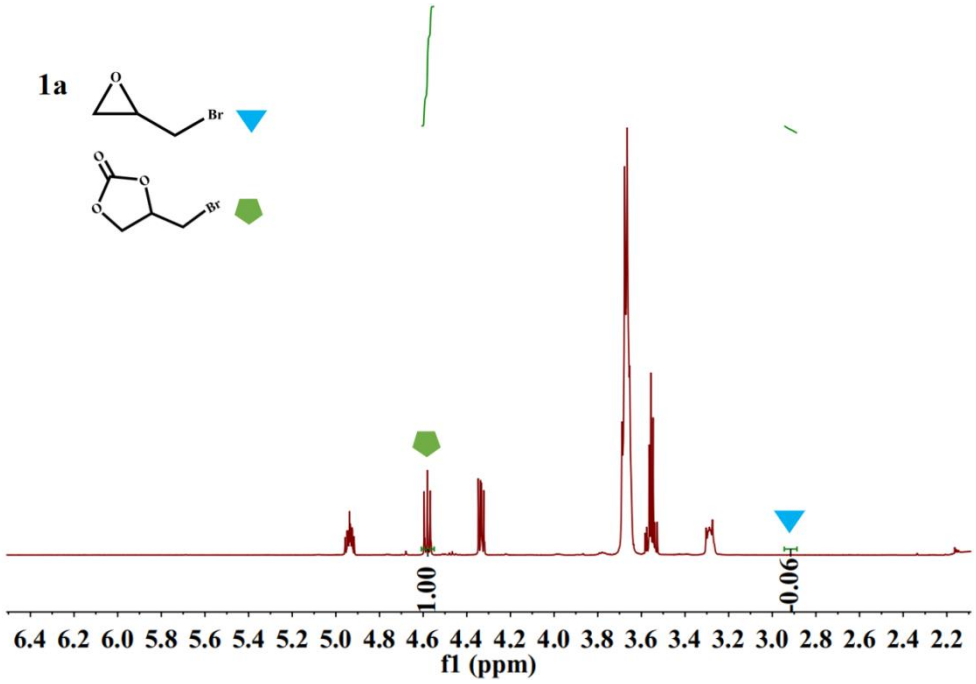

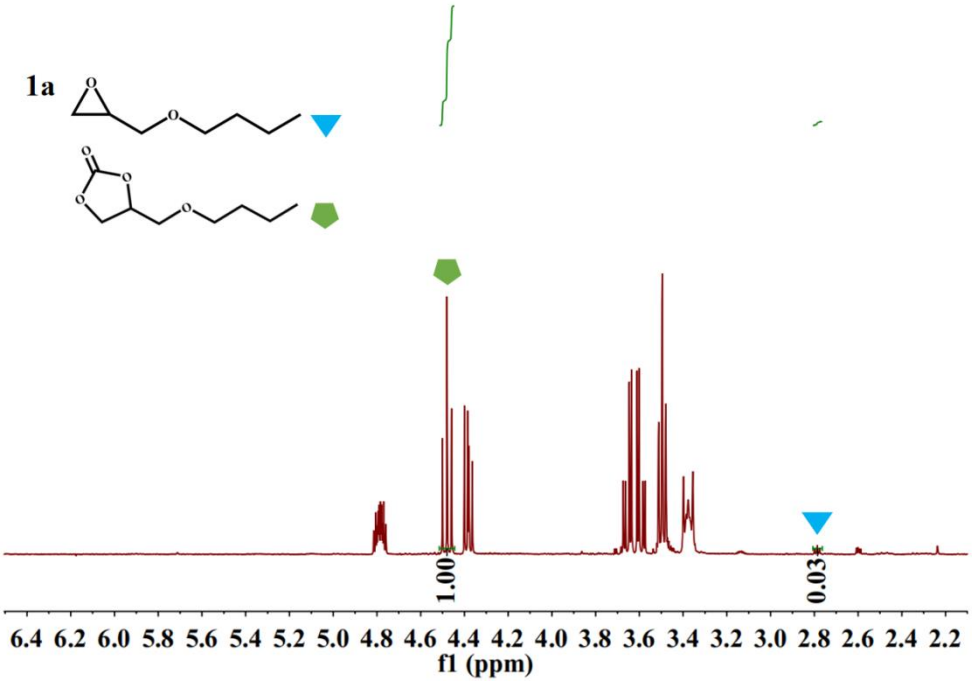
1a
1.00
0.03
6.4 6.2 6.0 5.8 5.6 5.4 5.2 5.0 4.8 4.6 4.4 4.2 4.0 3.8 3.6 3.4 3.2 3.0 2.8 2.6 2.4 2.2
f1 (ppm)

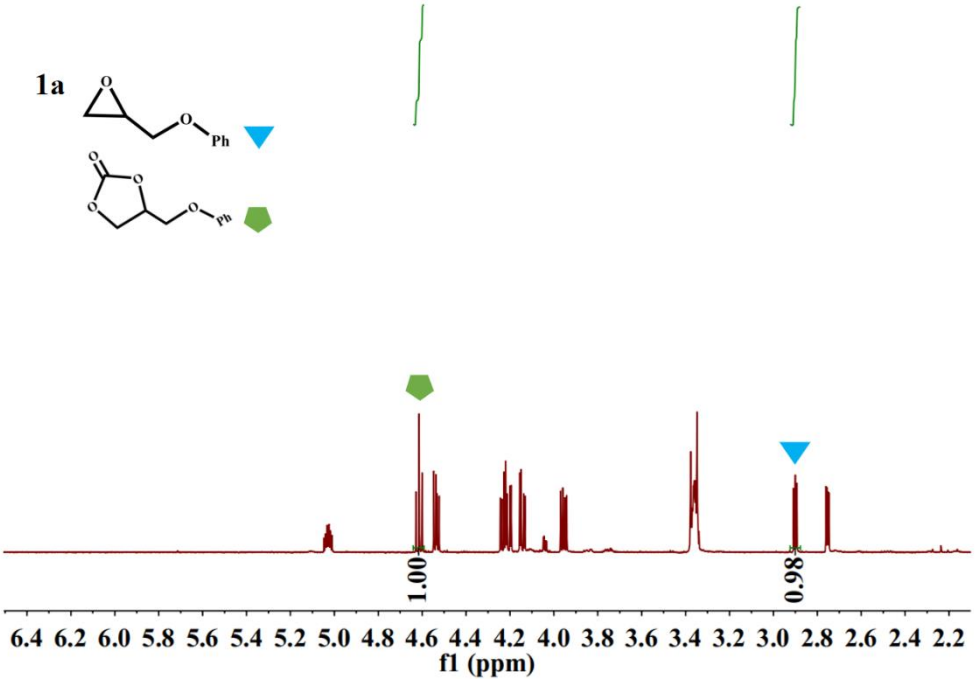
1a
Ph
1.00
0.98
6.4 6.2 6.0 5.8 5.6 5.4 5.2 5.0 4.8 4.6 4.4 4.2 4.0 3.8 3.6 3.4 3.2 3.0 2.8 2.6 2.4 2.2
f1 (ppm)

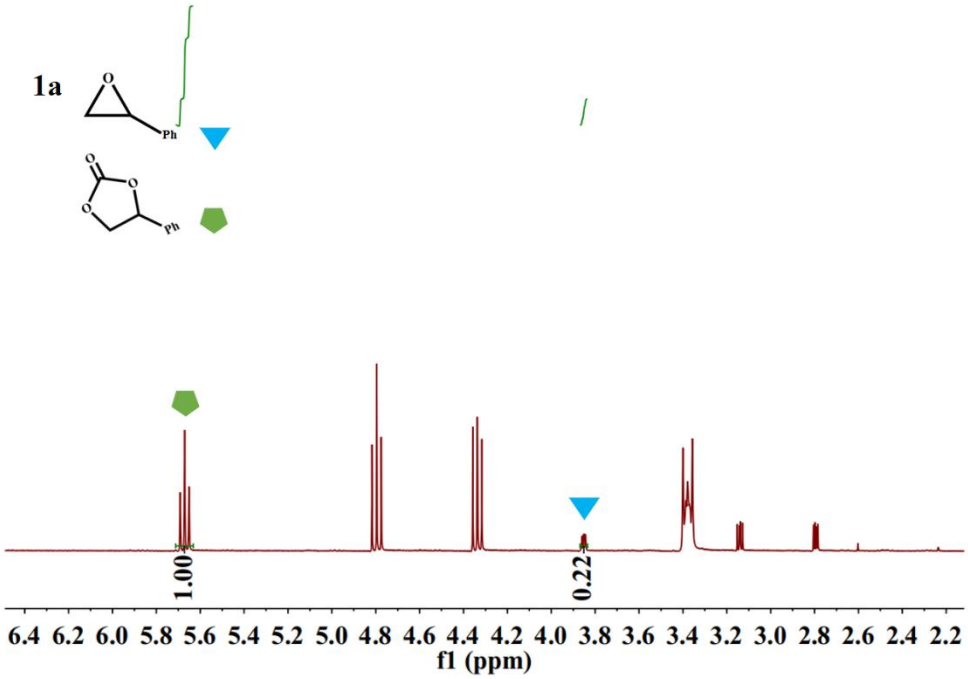
1a
Ph
Ph
1.00
0.22
6.4 6.2 6.0 5.8 5.6 5.4 5.2 5.0 4.8 4.6 4.4 4.2 4.0 3.8 3.6 3.4 3.2 3.0 2.8 2.6 2.4 2.2
f1 (ppm)

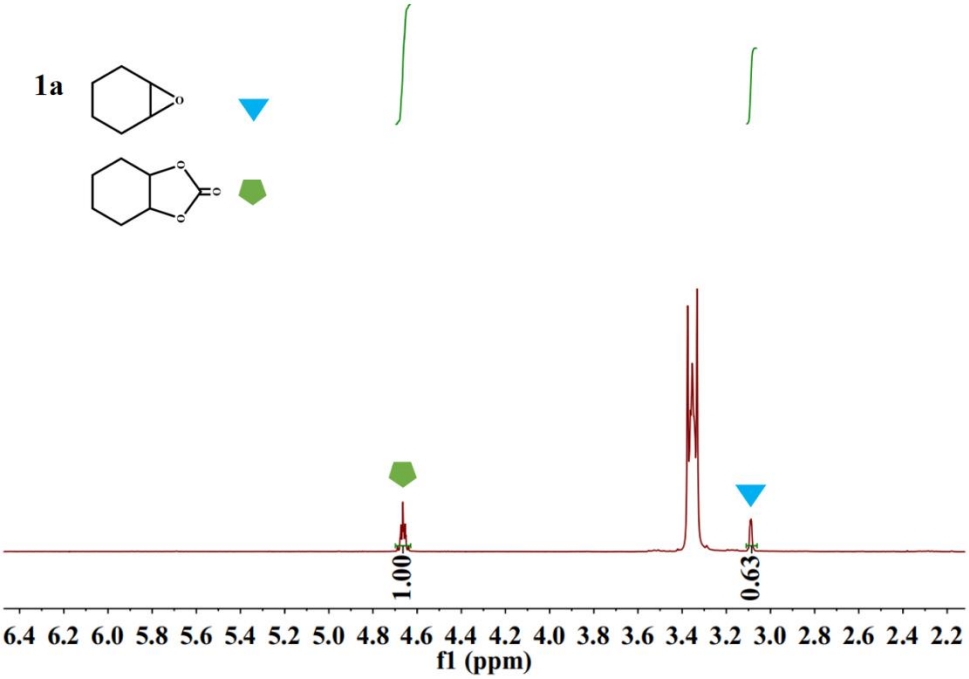
1a
1.00
0.63
6.4 6.2 6.0 5.8 5.6 5.4 5.2 5.0 4.8 4.6 4.4 4.2 4.0 3.8 3.6 3.4 3.2 3.0 2.8 2.6 2.4 2.2
f1 (ppm)

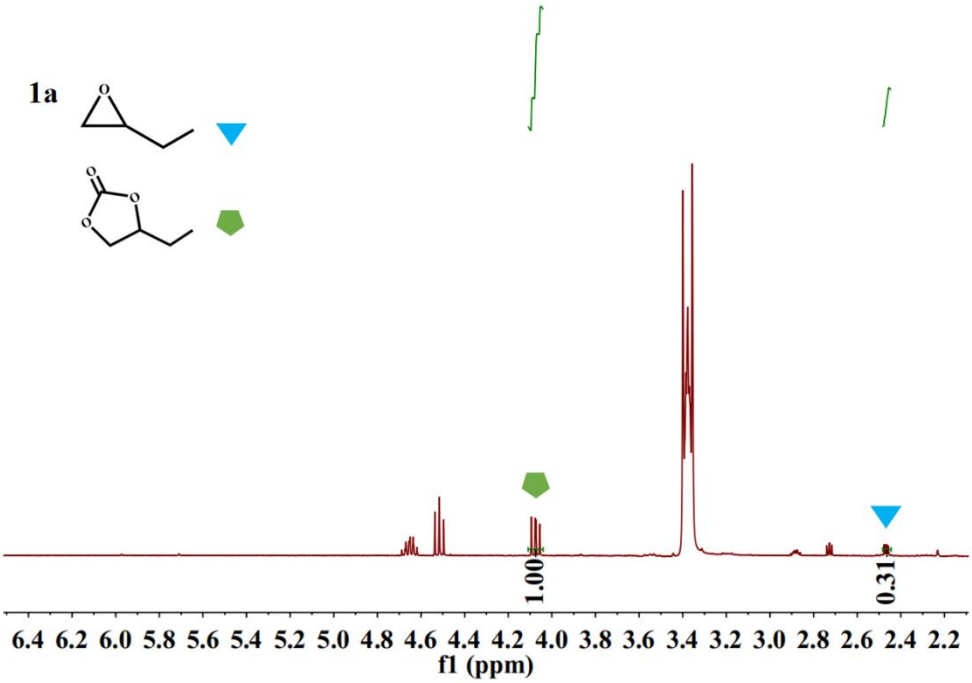


**Fig**. **S22** $^{1}$H NMR spectrum of cyclic carbonate with **1a**.

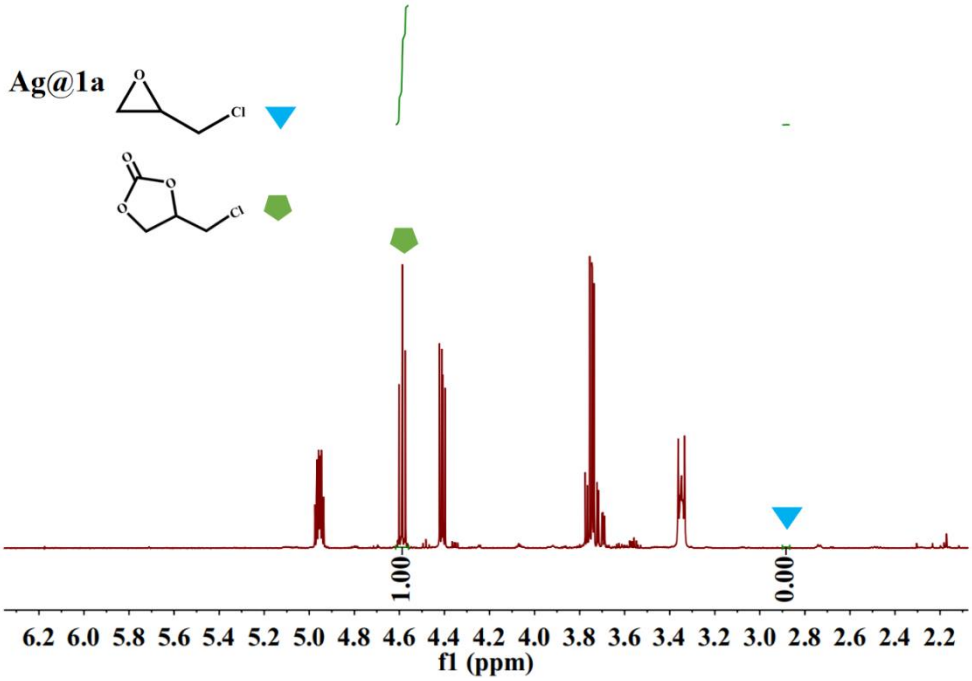

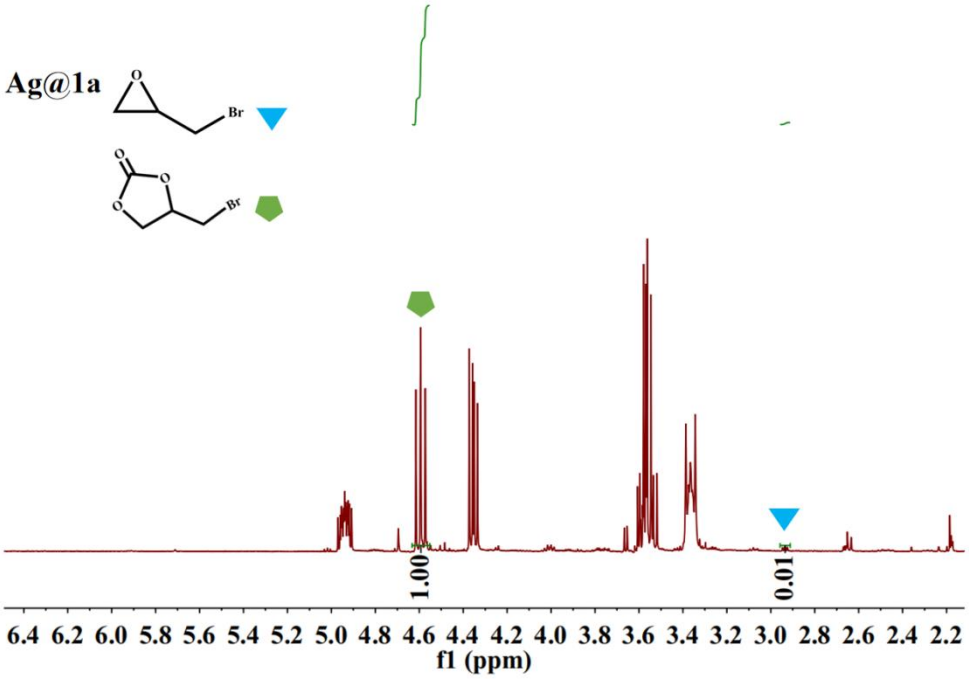
Ag@1a
Br
Br
1.00
0.01
6.4 6.2 6.0 5.8 5.6 5.4 5.2 5.0 4.8 4.6 4.4 4.2 4.0 3.8 3.6 3.4 3.2 3.0 2.8 2.6 2.4 2.2
f1 (ppm)

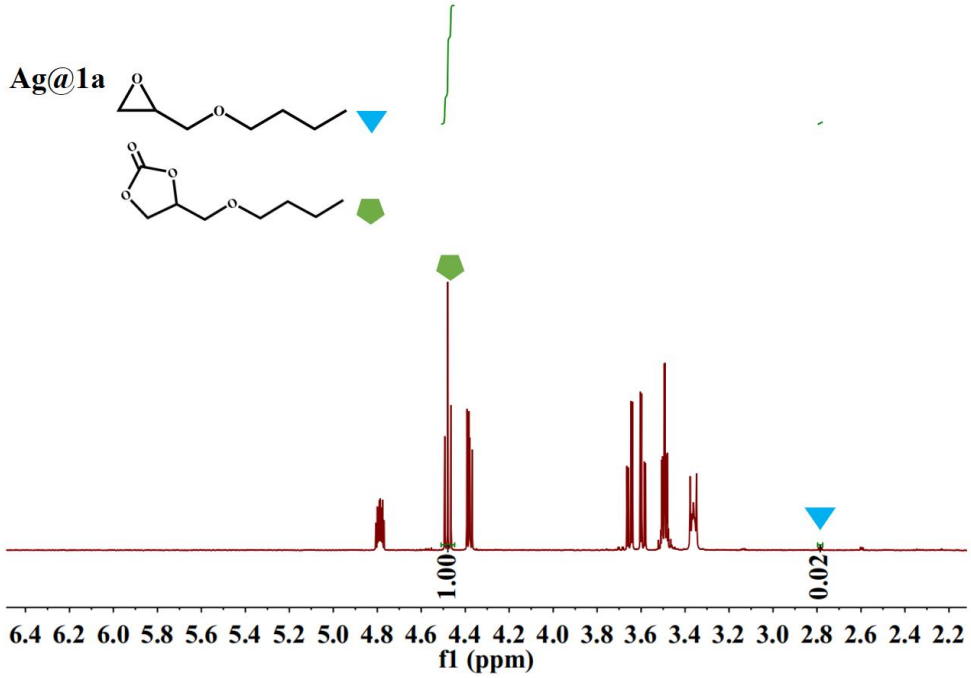
Ag@1a
1.00
0.02
6.4 6.2 6.0 5.8 5.6 5.4 5.2 5.0 4.8 4.6 4.4 4.2 4.0 3.8 3.6 3.4 3.2 3.0 2.8 2.6 2.4 2.2
f1 (ppm)

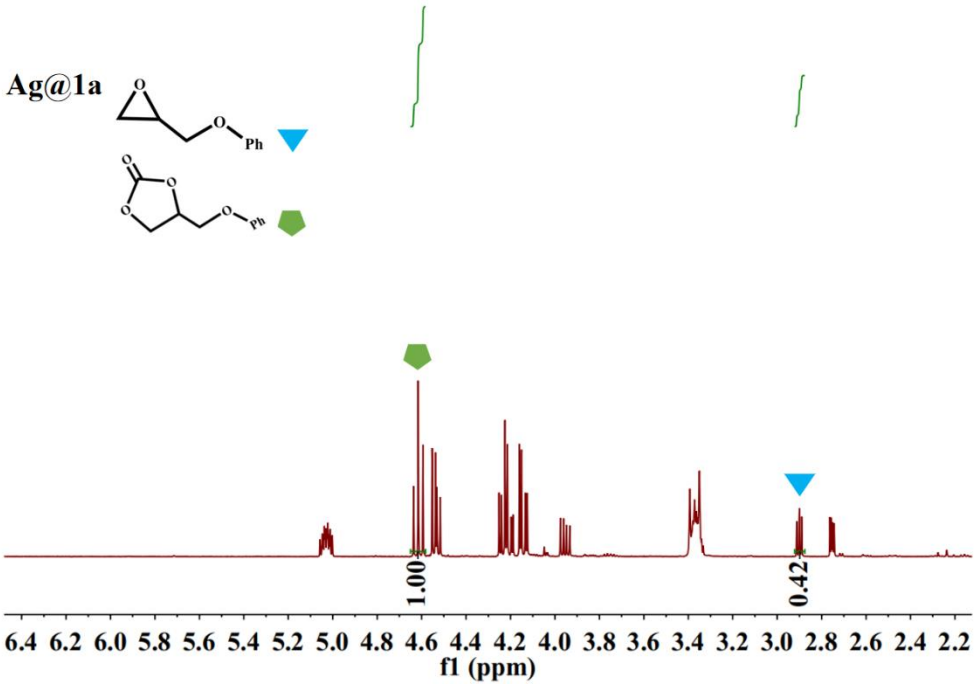
Ag@1a
Ph
Ph
1.00
0.42
6.4 6.2 6.0 5.8 5.6 5.4 5.2 5.0 4.8 4.6 4.4 4.2 4.0 3.8 3.6 3.4 3.2 3.0 2.8 2.6 2.4 2.2
f1 (ppm)

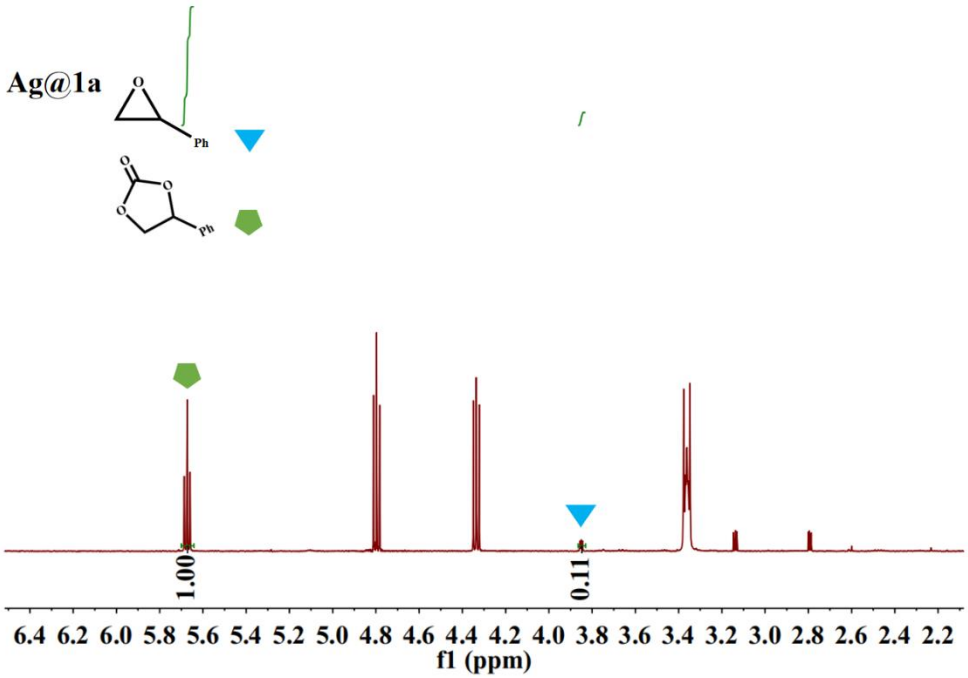
Ag@1a
Ph
Ph
1.00
0.11
6.4 6.2 6.0 5.8 5.6 5.4 5.2 5.0 4.8 4.6 4.4 4.2 4.0 3.8 3.6 3.4 3.2 3.0 2.8 2.6 2.4 2.2
f1 (ppm)

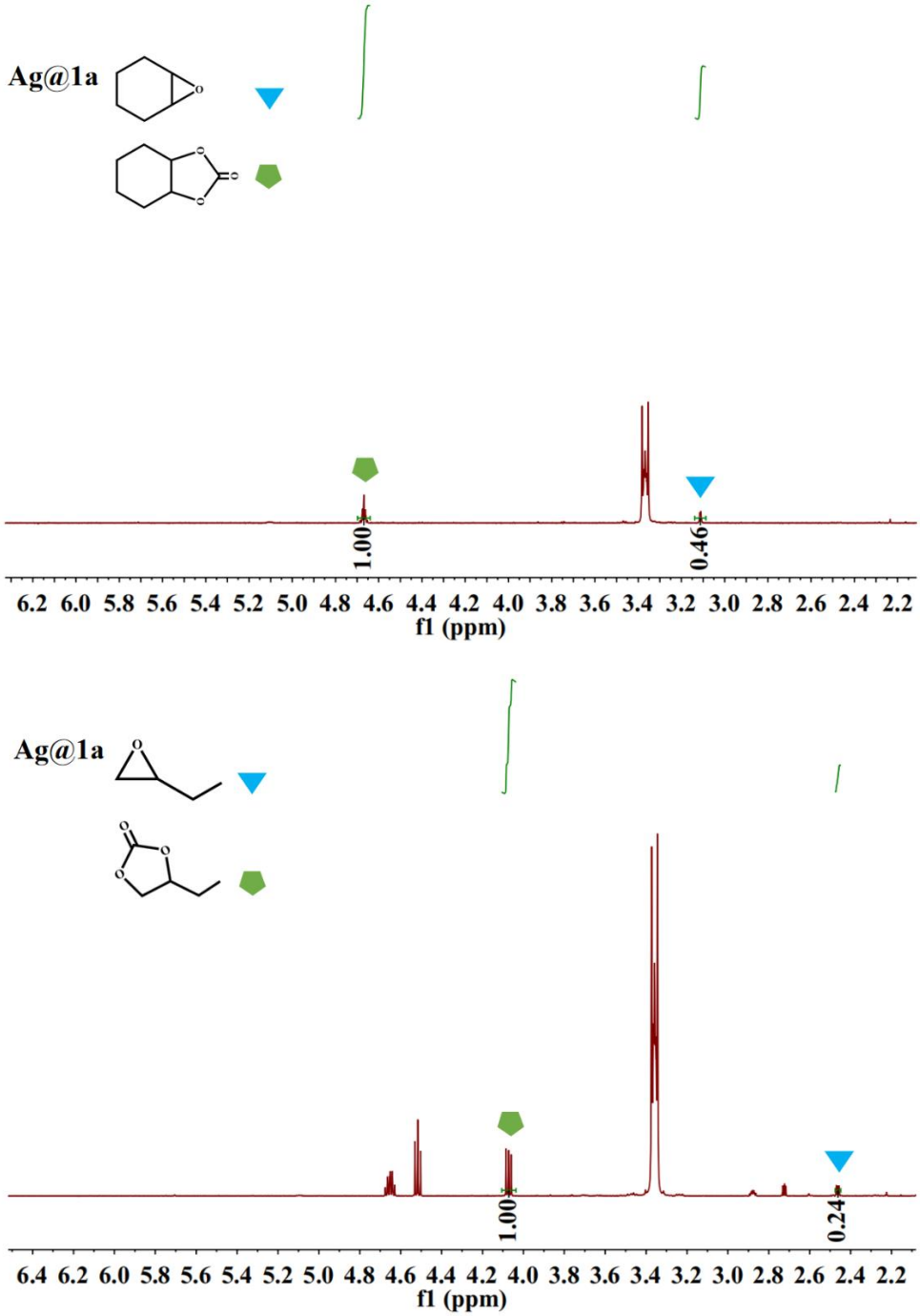


**Fig**. **S23** $^{1}$H NMR spectrum of cyclic carbonate with Ag@**1a**.

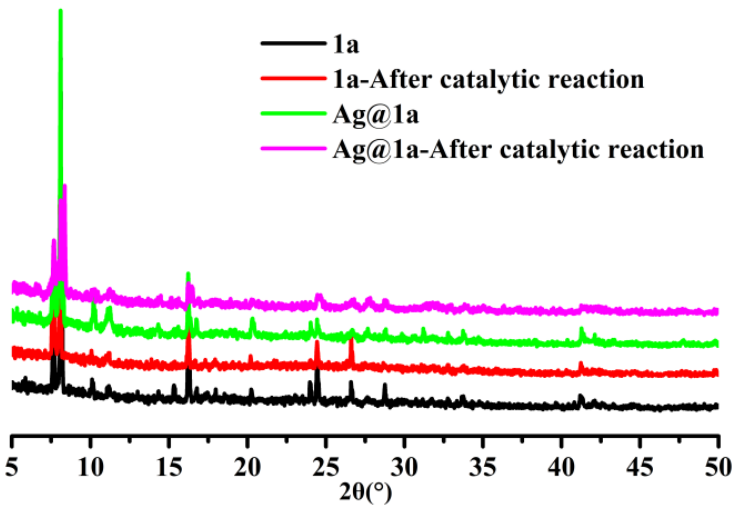


**Fig. S24** PXRD patterns of **1** and Ag@**1** after catalytic reaction, respectively.

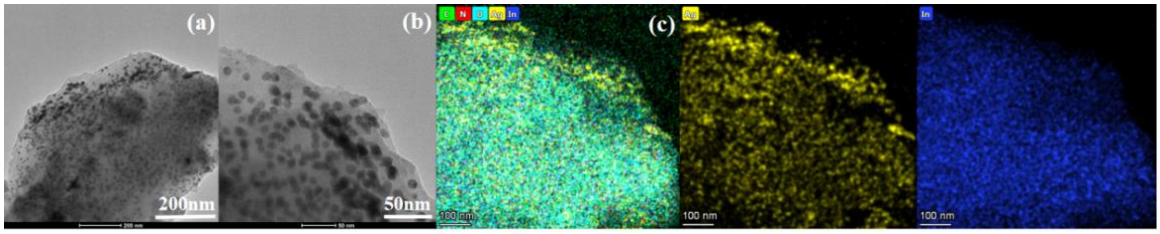


**Fig**. **S25** TEM images of Ag@**1** after catalytic reaction.

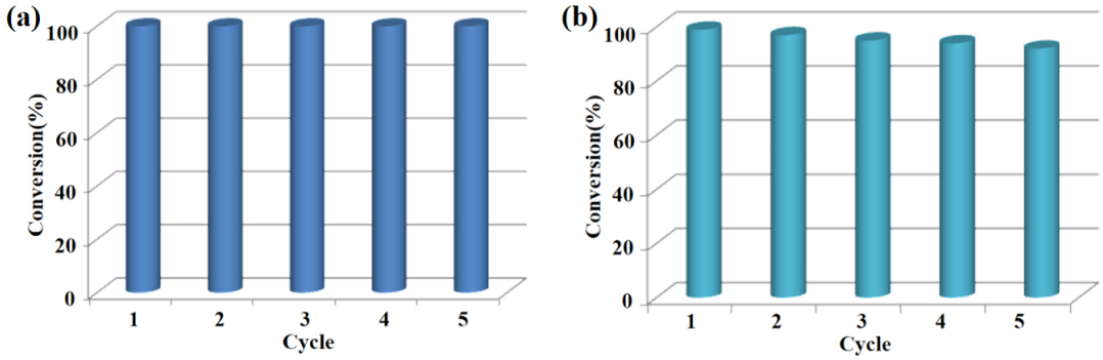


**(a)** **(b)**

**Fig**. **S26** Recycle experiments of **1a** (a) and Ag@**1a** (b) for the cycloaddition of $CO_2$ and epichlorohydrin , respectively.

## S7. References

1. X. J. Kong, Y. Z. Zhang, T. He, X. Q. Wu, M. M. Xu, S. N. Wang, L. H. Xie and J. R. Li, *CrystEngComm*, 2018, **20**, 6018-6025.

2. X. Duan, R. Lv, Z. G. Ji, B. Li, Y. J. Cui, Y. Yang and G. D. Qian, *Inorg. Chem. Front.*, 2018, **5**, 1193-1198.

3. J. E. Reynolds III, K. M. Walsh, B. Li, P. Kunal, B. L. Chen and S. M. Humphrey, *Chem. Commun.*, 2018, **54**, 9937-9940.

4. Y. T. Li, J. W. Zhang, H. J. Lv, M. C. Hu, S. N. Li, Y. C. Jiang and Q. G. Zhai, *Inorg. Chem.*, 2020, **59**, 10368-10373.

5. H. P. Li, S. N. Li, H. M. Sun, M. C. Hu, Y. C. Jiang and Q. G. Zhai, *Cryst. Growth Des.*, 2018, **18**, 3229-3235.

6. J. W. Zhang, P. Qu, M. C. Hu, S. N. Li, Y. C. Jiang and Q. G. Zhai, *Inorg. Chem.*, 2019, **58**, 16792-16799.

7. D. J. Bai, Y. Wang, M. H. He, X. X. Gao and Y. B. He, *Inorg. Chem. Front.*, 2018, **5**, 2227-2237.

8. Y. B. He, Z. J. Zhang, S. C. Xiang, F. R. Fronczek, R. Krishna and B. L. Chen, *Chem. Eur. J.*, 2012, **18**, 613-619.

9. J. Liu, G. P. Yang, J. Jin, D. Wu, L. F. Ma and Y. Y. Wang, *Chem. Commun.*, 2020, **56**, 2395-2398.

10. L. X. You, S. X. Yao, B. B. Zhao, G. Xiong, I. Dragutan, V. Dragutan, X. G. Liu, F. Ding and Y. G. Sun, *Dalton Trans.*, 2020, **49**, 6368-6376.

11. H. J. Lv, Y. P. Li, Y. Y. Xue, Y. C. Jiang, S. N. Li, M. C. Hu and Q. G Zhai. *Inorg. Chem.*, 2020, **59**, 4825-4834.

12. B. Zhang, Q. Q. Chu, K. F. Yue, S. H. Zhang, B. Liu and Y. Y Wang. *Inorg. Chem.*, 2019, **58**, 4019-4025.

13. Q. Q. Chu, B. Zhang, H. H. Zhou, B. Liu, L. Hou and Y. Y Wang. *Inorg. Chem.*, 2020, **59**, 2853-2860.

14. B. Zhang, P. Y. Guo, L. N. Ma, B. Liu, L. Hou and Y. Y. Wang. *Inorg. Chem.*, 2020, **59**, 5231-5239.

15. Z. Y. Li, Y. X. Ye, Z. Z. Yao, J. Z. Guo, Q. J. Lin, J. D. Zhang, Z. J. Zhang, F. F. Wei and S. C. Xiang. *J. Mater. Chem. A*, 2018, **6**, 19681-19688.

16. Z. J. Guo, J. M. Yu,Y. Z. Zhang, J. Zhang, Y. Chen, Y. F. Wu, L. H. Xie and J. R. Li. *Inorg. Chem.*, 2017, **56**, 2188-2197.

17. B. Zhang, S. H. Zhang, B. Liu, K. F. Yue, L. Hou and Y. Y. Wang. *Inorg. Chem.*, 2018, **57**, 15262-15269.

18. L. Z. Liu, Z. Z. Yao Y. X., Ye, Y. K. Yang, Q. J. Lin, Z. J. Zhang, M. O'Keeffe and S. C. Xiang. *J. Am. Chem. Soc.*, 2020, **142**, 9258-9266.

19. K. Liu, X. Li, D. X. Ma, Y. Han, B. Y. Li, Z. Shi, Z. J. Li and L. Wang. *Mater. Chem. Front.*, 2017, **1**, 1982-1988.